MULTIPLE FOCUS REFLECTANCE CONFOCAL MICROSCOPY FOR IN VIVO

IMAGING

A Dissertation

by

CORY ALLAN OLSOVSKY

Submitted to the Office of Graduate and Professional Studies of
Texas A&M University
in partial fulfillment of the requirements for the degree of

DOCTOR OF PHILOSOPHY

Chair of Committee,	Kristen Maitland
Co-Chair of Committee,	Brian Applegate
Committee Members,	Javier Jo
	Philip Hemmer
Head of Department,	Anthony Guiseppi-Elie

May 2017

Major Subject: Biomedical Engineering

ABSTRACT

Light microscopy techniques provide a means to image interesting features on the very small scale. Advances in passive and active optical elements have driven progress in microscopy, including but not limited to super-resolution, large field of view, and three-dimensional microscopy. Medical diagnostics can benefit from this progress. Typically, for a suspected cancerous tissue, a biopsy is taken and analyzed by histology. Features of the tissue can be identified throughout the depth of the slice to inform diagnosis. Translating optical techniques to clinical applications presents a unique challenge. Typically, a microscopy sample is cut, sliced, and stained as part of the preparation needed for benchtop microscopes. In the clinic, the sample is inaccessible within a living, breathing human subject. Confocal microscopy is a well known technique that can solve part of the problem, as it can image thin slices of tissue optically (i.e. no cutting necessary). Additionally, as a reflectance microscope, no exogenous contrast agents are needed. However, current techniques have not shown to be effective for imaging the entire tissue due to the cumbersome nature of in vivo imaging.

This dissertation reports solutions by designing a confocal microscope capable of imaging live bulk tissue at multiple depths by means of some non-mechanical tunable focus. First, we evaluate the technique, chromatic confocal microscopy, to simultaneously capture images at multiple depths. We present a chromatic confocal microscope with expanded range that can produce images from a highly scattering tissue sample. Design considerations and future work are discussed. Second, we discuss the use of a hand-held confocal microscope which employs a tunable lens for multi-depth imaging and present a second generation alignment-free design with improved image quality. Image quality and reliability are paramount to validating an imaging system for use as a clinical diagnostic

tool. We show the capability of the system to detect features by means of optical biopsy and compare these images to the actual histological analysis.

DEDICATION

To Brooke

ACKNOWLEDGMENTS

I would like to thank Dr. Kristen Maitland for mentoring me the past six years. Without her guidance and patience, this work would not have possible. I also appreciate the many conversations with Dr. Brian Applegate and his mentorship. I thank the other members of my committee, Dr. Javier Jo and Dr. Phillip Hemmer, for their support as well. All of you have been an inspiration to me during the pursuit of my Doctorate. I want to also acknowledge Drs. Lisa Cheng and John Wright, our collaborators at Texas A&M University Baylor College of Dentistry, for their support and discussions on this work. They are instrumental to our understanding of cancer histopathology and achieving the results in this work.

I thank all of my fellow graduate students who have provided friendship and many philosophical and intellectual discussions. Especially thanks to my good friends and colleagues: Taylor Hinsdale, Scott Mattison, Bilal Malik, Joel Bixler, Esteban Carbajal, Madeleine Durkee, Rodrigo Cuenca, Joey Jabbour, Meagan Saldua, Ryan Shelton, and Oscar Carrasco . I also would like to thank my close friend and colleague Tony Boyle. This work would also have not been possible without the support of the Association of Former Students Graduate Merit Fellowship and the National Science Foundation Graduate Research Fellowship. I also thank Dr. Hope Beier for giving me the opportunity to perform research at the Air Force Research Laboratory and the Repperger Internship program which supported my work.

I must thank my family for supporting me through the 21st grade of schooling. Each of you have shaped me in ways you may not know. My father, Mark, is one of the truly smartest people I know and has always been an inspiration. My mother, Mary, also inspirational to my curiosity and forever supportive. I've inherited my sense of respect,

generosity, and determination from my stepfather, Dub, who I love. I've received much support from my aunt, Sandi, and uncle, Kirby, each of whom I strive to be like. They are as close to me as my own parents. I thank my grandparents, Valerie and Al Olsovsky, for giving me the most support even though they would most like to see me back home with them. I thank my brothers and sister, Erik, Paul, and Bethany, and especially Erik for taking care of me. I am proud of all of them. I also want to give special thanks to my uncle, John, for inspiring my curiosity and skepticism.

I want to acknowledge and thank my wife, Brooke, who has supported me day to day. It is to her that I owe this work, as she is the one who motivates me to better myself and to contribute to the broader community. Also special thanks to her family, my family. Her Mother and Father have been my own. And finally I acknowledge my nieces, Lizzie and Maddie, who I aim to inspire.

CONTRIBUTORS AND FUNDING SOURCES

Contributors

Funding Sources

TABLE OF CONTENTS

LIST OF FIGURES

LIST OF TABLES

1. INTRODUCTION

1.1 Motivation

This work aims to improve cancer survivability by improving early diagnosis of epithelial cancers, specifically oral cancer. Confocal microscopy is desired as a diagnostic tool for stomatology, however, limitations such as motion artifact and inaccessibility of tissues prevent further use of most devices. Some studies have been performed but the need for more research is cited [2, 3]. We propose to develop techniques which allow stable depth positioning for in vivo confocal microscopy. Additionally, we develop a system which achieves oral cavity imaging in difficult to reach locations with minimal motion artifact.

1.1.1 Oral Cancer

Although oral cancer comprises only 4% of new cases of cancer, oral cancer survival rates are critically low at 66%, compared with survival rates of the most common cancers (Prostate at 99% and Breast at 91%) [4]. The low survivability is in part due to late detection of oral cancer [5]. Recently, oral cancer diagnoses have increased in young people [6]. Early detection of cancer could further raise survivability.

Epithelium has several characteristic layers (Figure 1.1) [7]. The top of the squamous epithelium (corneal and granular layers) exhibit flat cells with some anuclear and nuclear cells. Below these layers in the spinous layer which can be thick (up to several hundred microns). At the junction of epithelium and submucosa is the basement membrane. Cells divide at the basement membrane and move to the surface. It is here at this junction that squamous cell carcinoma can first present, as the cells overdivide. The figure shows dysplasia where cells are numerous and large in the lower layers of the epithelium. Analyzing features at different depths can help to stage premalignancy or determine malignant versus benign.

1
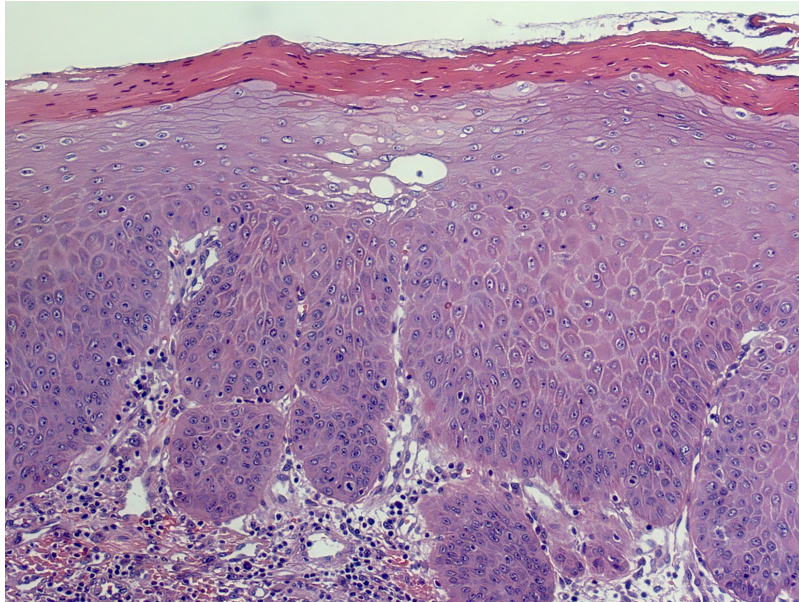
Figure 1.1: Dysplasia of the epithelium of the oral cavity.

1.2   Optical Microscopy

Optical microscopy offers many techniques for obtaining diagnostic information. For oral cancer, there are reflective and fluorescence techniques. A current standard for visual inspection is to use toluidine blue, a dye, which is used to determine cancerous vs benign tissue, albeit with only a positive predictive value of 35% [8]. Other techniques use autofluorescence photography [9], however these only intend to be screening for biopsies. Current studies attempt to utilize the autofluorescence of oral mucosa to correlate difference in metabolic molecules to cancerous tissue [10].

Other optical techniques utilize the reflectance of tissue features derived from changes in refractive index between different cell parts. A popular technique, optical coherence tomography (OCT), has been used for oral cancer imaging [11]. OCT can have superior axial resolution (<10 microns), but is generally low resolution in the lateral dimension. High NA optics can be used to achieve high lateral resolution, but the resulting system

would be very similar to a confocal microscope, as the depth of field would limit the range to that of confocal, albeit with slightly better axial resolution for very wide band OCT systems. Reflectance confocal microscopy (RCM) is a simple technique requiring a pinhole as a spatial filter for obtaining high resolution optical sections in bulk tissue. The complexity comes from the laser scanning capabilities. RCM has been used for oral cancer recently [12, 13], including this work which adds the capability of non-mechanical axial scanning.

1.3 Translational Challenges

Although many optical techniques have been developed for imaging biological samples and even in vivo, there remain challenges to translating these techniques to be used in the clinic. Motion artifact is one challenge that many different techniques attempt to avoid. Optical imaging devices used for in vivo imaging such as endoscopes and rigid scopes are hand held devices. Because of this, the shaking of the hand or movement of the patient can lead to blurring since the time an image takes to be captured is longer than the time the scope moved from one position or angle to another. Imaging speed is highly desired to avoid motion artifact, so fast moving laser scanning optics are typically used. These systems can add size, so other techniques discussed later try to obviate the need for these scanning modules. Although made for imaging ex vivo skin excisions, one technique tries to stitch images together [14] which can be very useful even in a hand held device. Another feature is desired for clinical use: miniaturization. Many areas of the body are difficult to reach such as the colon, esophagus, or cervix. The oral cavity is slightly more accessible due to the proximity of the outside of the body, but the teeth and jaw can add unique difficulty to accessibility. Development of optics has shown the desire for miniature systems include miniaturized lenses [15], miniature scanning optics (MEMS) [16], and fiber based systems [17, 18]. In addition to these design challenges, a device to be used

3

in humans must be sterile. As well it should be comfortable to the operator which can affect motion and motion artifact. Additionally, an imaging procedure must be brief and practical to not encumber the standard of care.

1.4 Conclusion

This work aims to develop confocal scanning techniques for fast axial scanning and improved axial positioning. Additionally, a confocal microscopy device is used in a clinical study to demonstrate efficacy of confocal microscopy for epithelial imaging. The results of the study also benefit the scientific community as it builds a database of correlated histology and optical histology of various types of oral lesions.

2. CONFOCAL MICROSCOPY

2.1 History and Technique

The scanning confocal microscope was invented in 1955 and patented in 1957 by Marvin Minsky [19]. In his memoirs, he notes that, while studying the biology of the brain during his graduate and post graduate studies, he was frustrated that the current technology would not allow him to study the three-dimensional structure of the brain – bulk nervous tissue – due to scattering in thick samples. One day he realized that the unwanted light could be controlled by imaging a pinhole onto the sample (and subsequently collecting the light through a pinhole). The instrument (Figure 2.1), along with a stage scanning mechanism built with two orthogonal electronically controlled "tuning forks", was dubbed the "Double focusing stage scanning microscope" [1]. Fifteen years later, after the development of the laser, the first laser scanning confocal microscope is described [20]. Since then, the confocal laser scanning microscope has been used as a useful instrument in biological research, and has promising use as a medical diagnostic tool.

2.1.1 Theory of Operation

The confocal laser scanning microscope can be described using geometric optics as well as Fourier optics. The geometric optics explanation is illustrated in Figure 2.2. The point source is typically either a spatially filtered extended source, such as an arc lamp, or a single mode laser beam (i.e. TEM_{00}). Using a point source will ensure that the illumination in an ideal system (one where light is only affected by ideal optics) will have a focal size which is limited by the point spread function of the optics. In the schematic, a beam splitter is used so that the illumination and detection use the same objective. Illumination light passes through the beam splitter to the objective, and back reflected light passes back through the objective and is reflected by the beam splitter onto the pinhole. The illustration
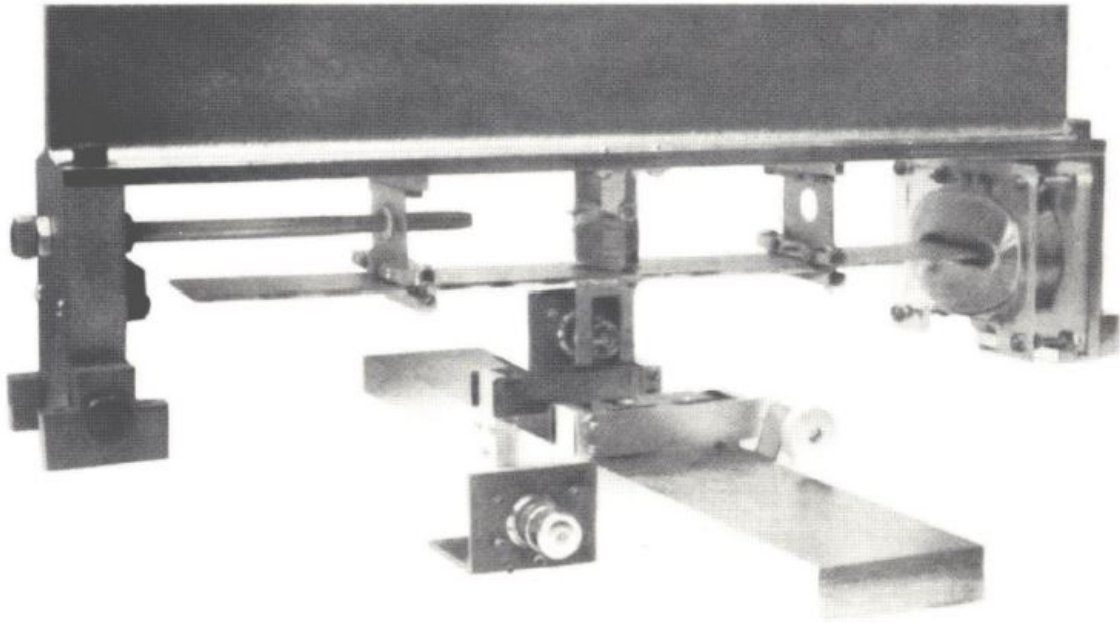
Figure 2.1: Photo of original confocal microscope, photographed in 1988 by Minsky. This figure is reproduced from [1] with permission from John Wiley and Sons (License No: 3936640027425)

shows the path for rays which are reflected from the focal plane (solid lines) and rays which are reflected from an out of focus plane (dashed lines). The in focus rays pass through the pinhole and are detected, whereas the out of focus rays are mostly blocked by the sides of the pinhole.

The theory of operation of a confocal microscope can be explained using Fourier optics theory. This analysis helps to approximate the actual resolution performance of a confocal system. The system is assumed to be some form of partially coherent system, as in Figure 2.2, where the pinhole is real and finite in size, or is a multimode fiber. For systems using a single mode fiber for the detection pinhole, the detection is fully coherent and is described in detail by Gu [21]. To model the performance of the system, we must first model the point spread function of the lens [22]. The lens is approximated by an ideal thin lens with
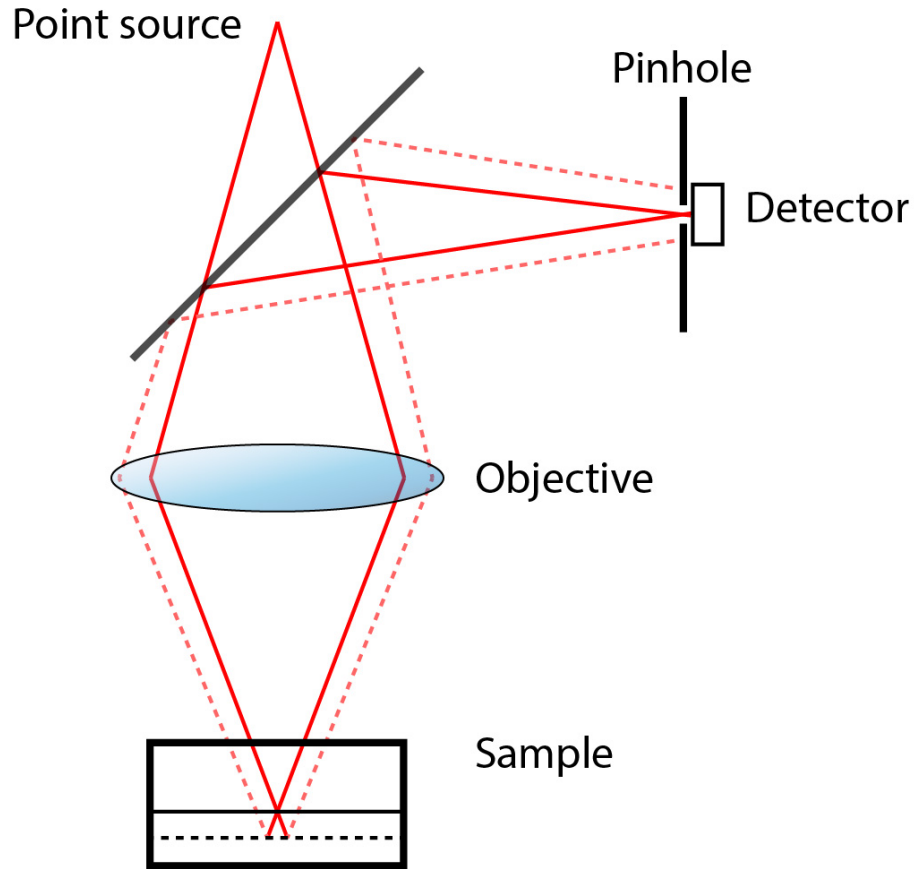
Figure 2.2: Schematic of simple confocal microscope with a point source, beam splitter, objective, and pinhole detector. The solid shows the path of light converging on the conjugate focal points of the point source, sample focus, and pinhole. The dashed line shows light back reflected from an out of focus region, which is mostly blocked by the pinhole. Note: only the marginal rays are shown.

a phase transformation,

$$t(x,y) = exp\left(\frac{jk}{2f}(x^2 + y^2)\right) \tag{2.1}$$

where f is the focal length of the lens and k is the wave number. The lens also has an

aperture defined by the pupil function $P(x,y)$. The point spread function described how

a lens transforms a point source, or inversely, how it will transform a plane wave. If

we only look at coordinates sufficiently close the optical axis, we can apply the Fresnel

approximation of the Kirchhoff diffraction formula to model the complex amplitude of the plane wave transformed by the lens which has propagated some distance z,

$$U(x_2, y_2) = \frac{exp(-jkz)}{j\lambda z} \iint_{-\infty}^{+\infty} P(x_1, y_1) exp\left(\frac{jk}{2f}(x_1^2 + y_1^2)\right)$$
$$\times exp\left(\frac{-jk}{2z}\{(x_2 - x_1)^2 + (y_2 - y_1)^2\}\right) dx_1 dy_1 \tag{2.2}$$

where x_1 and y_1 are coordinates of the plane immediately after the lens, and x_2 and y_2 are coordinates of the plane at distance z. Normally, we are interested in the wave at the focal plane where $z = f$ and equ. 2.2 reduces to the Fourier transform of the pupil function. However, we want to allow a small amount of defocus to analyze the axial response, and so z and f remain distinct. At this point, we will assume radial symmetry (as most lenses are circularly symmetric), and collect the terms,

$$U(r_2) = \frac{exp(-jkz)}{j\lambda z} exp\left(\frac{j\pi r_2^2}{\lambda z}\right)$$
$$\times \int_0^\infty P(r_1) exp\left\{\frac{jkr_1^2}{2}\left(\frac{1}{f} - \frac{1}{z}\right)\right\} J_0\left(\frac{2\pi r_1 r_2}{\lambda z}\right) 2\pi r_1 dr_1 \tag{2.3}$$

For a more generalized equation, we can use normalized units for the pupil plane and the space around the plane near distance z,

$$\rho = \frac{r_1}{a} \tag{2.4}$$

$$v = kr_2 sin(\alpha) \tag{2.5}$$

where ρ is the normalized pupil coordinate which ranges from zero to one, a is the pupil radius, v is the normalized radial coordinate near the focus, and α is the half angle of the cone of light collected by the lens. For small angles and restricting z to near the focus,

$sin(\alpha) \approx a/z \approx a/f$. Equ. 2.3 can then be written as,

$$
\begin{aligned}
U(v) =& \frac{-j2N}{a} exp(-jkz) exp\left(\frac{jv^2}{4N}\right) \\
& \times \int_0^1 exp\left\{\frac{jk\rho^2 a^2}{2}\left(\frac{1}{f} - \frac{1}{z}\right)\right\} J_0(v\rho)\rho d\rho
\end{aligned}
\tag{2.6}
$$

where N is the Fresnel number,

$$
N = \frac{\pi a^2}{\lambda z}
\tag{2.7}
$$

If we define another normalized coordinate for the axial dimension,

$$
u = ka^2 \left(\frac{1}{f} - \frac{1}{z}\right)
\tag{2.8}
$$

then Equ. 2.6 as a function of u and v is,

$$
\begin{aligned}
U(u,v) =& \frac{-j2N}{a} exp(-jkz) exp\left(\frac{jv^2}{4N}\right) \\
& \times \int_0^1 exp(\tfrac{1}{2}ju\rho^2) J_0(v\rho)\rho d\rho
\end{aligned}
\tag{2.9}
$$

The optical axial coordinate u in Equ. 2.8 can be represented where the real coordinate is a deviation from the focus, δz, where $z = f + \delta z$. The optical axial coordinate can now be represented more familiarly as, $u = k\delta z sin^2(\alpha)$. The intensity is the modulus squared of the amplitude, which means the intensity will be proportional to the integral part of Equ. 2.9. So the general form of the point spread function $h(u,v)$ is,

$$
h(u,v) = \int_0^1 exp(\tfrac{1}{2}ju\rho^2) J_0(v\rho)\rho d\rho
\tag{2.10}
$$

Now the confocal intensity is simply the intensity point spread function of the illumination (assuming a point source) times the intensity point spread function of the detection path

convoluted with the finite pinhole. For a system using the same illumination and detection path, this is [23],

$$I = |h|^2(|h|^2 \otimes D) \tag{2.11}$$

where D is the detector aperture, or pinhole, which is typically defined by the function $circ(v/v_p)$ where v_p is the normalized pinhole radius. If we just consider a point at the focus, the point spread function is just $h(v) = J_1(v)/v$, where J_1 is the first order Bessel function of the first kind, and we can evaluate the intensity to find the half width of the point (which will be the definition of lateral resolution). The Matlab code for this is in Appendix A.1. The results for a set of pinhole sizes is plotted in Figure 2.3. Additionally, the signal level is plotted in Figure 2.4. The lateral point size is reduced for very small pinholes, though there is diminishing returns for values under 2. The resolution will slightly improve from there, however, signal is already below 50% and drops steeply. As the pinhole size is increased, the half width of the point tends to that of conventional microscopy [23]. The axial response can also be evaluated by integrating the PSF over the pinhole. In other words, what amount of light passes through the pinhole as a plane is translated through the axial dimension. So,

$$I = \int_0^{v_p} |h(2u, v)|^2 v dv \tag{2.12}$$

The values for half width of the axial response are plotted in Figure 2.5. Here a pinhole size below 2.5 does not significantly improve the sectioning capability. Clearly though, the pinhole size should be chosen close to the size of the Airy disk ($v_p \approx 3.8$) for good sectioning performance. For larger pinholes, there should still be good rejection of stray light and background from highly scattering samples, even if the focal volume is relatively large.

10
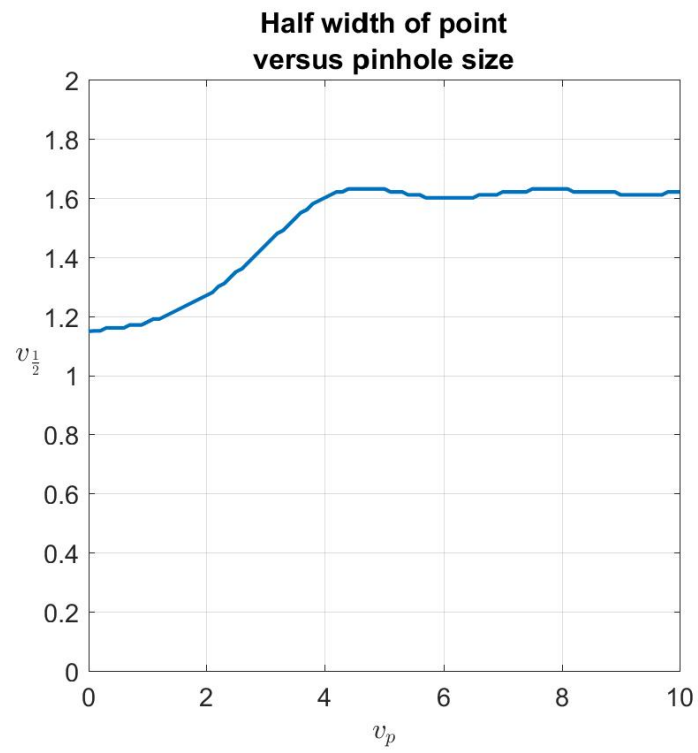
Figure 2.3: Theoretical half width of a point at the focus versus pinhole size

Confocal signal versus pinhole size
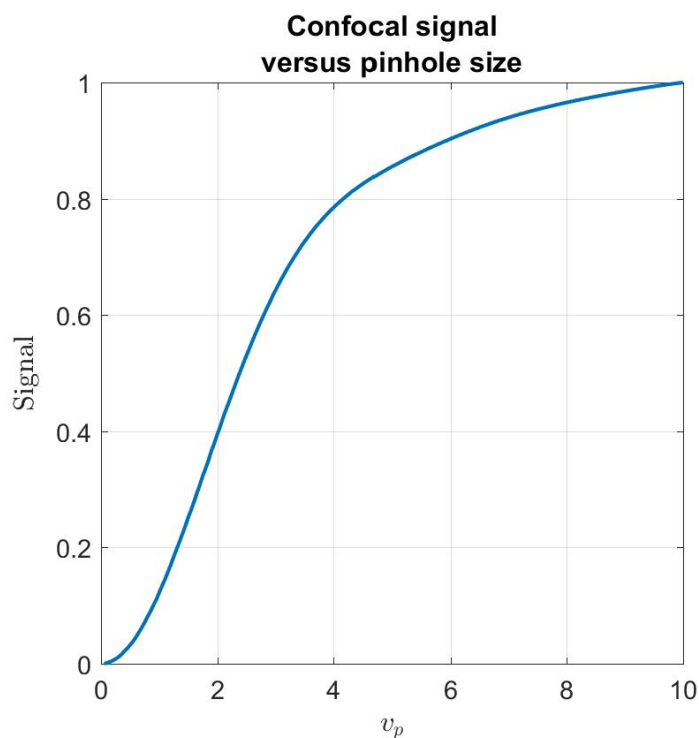
Figure 2.4: Theoretical confocal signal versus pinhole size

2.2 Variations and Clinical Application

There are many variation of confocal microscope. For example, other than stage scanning and laser scanning microscopes, as previously discussed, there is also the Nipkow scanning disk confocal microscope [24]. The Nipkow scanning disk is an arrangement of microlenses and pinholes in an Archimedes spiral pattern. The disk is used as an array of excitation and emission pinholes and is rotated very fast. This allows imaging speeds of up to 2000 frames per second. However, this technique is generally not as high resolution as laser scanning confocal systems because of the limited spacing of the pinholes on the disk. Closer spacing could result in pinhole crosstalk. There are many other variation of confocal microscopy. In the scope of this work, we can focus on innovations that lead toward clinically relevant applications. That is, to overcome the limitations of size

**Half width of axial response
versus pinhole size**
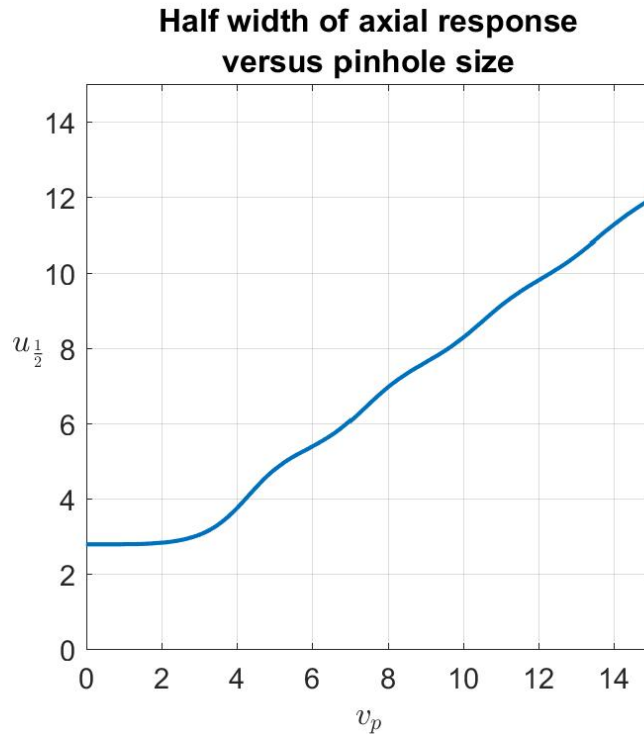
Figure 2.5: Theoretical axial half width versus pinhole size

constraint, highly scattering samples, and motion artifact.

The line scan confocal microscope is a confocal system which images an entire line at a time versus just a single point [25, 26]. Higher speed imaging can mitigate motion artifact and reduce scan time. This method uses a light source which is imaged as a line onto the sample, such as a laser focused by a cylindrical lens. The light is then imaged onto a linear sensor such as a line camera. Figure 2.6 shows a simple schematic of a line scan confocal system in the X-Z plane and Y-Z plane. This system uses a cylindrical lens to focus a laser in one dimension, resulting in a line focus. The line is then imaged by the detection arm onto a linear camera. The linear camera can be used as a slit, however, a physical slit mask can be used to improve resolution. Since a slit, or just line detector, is used, the light rejection is not as complete as it is for a pinhole. A slit allows light
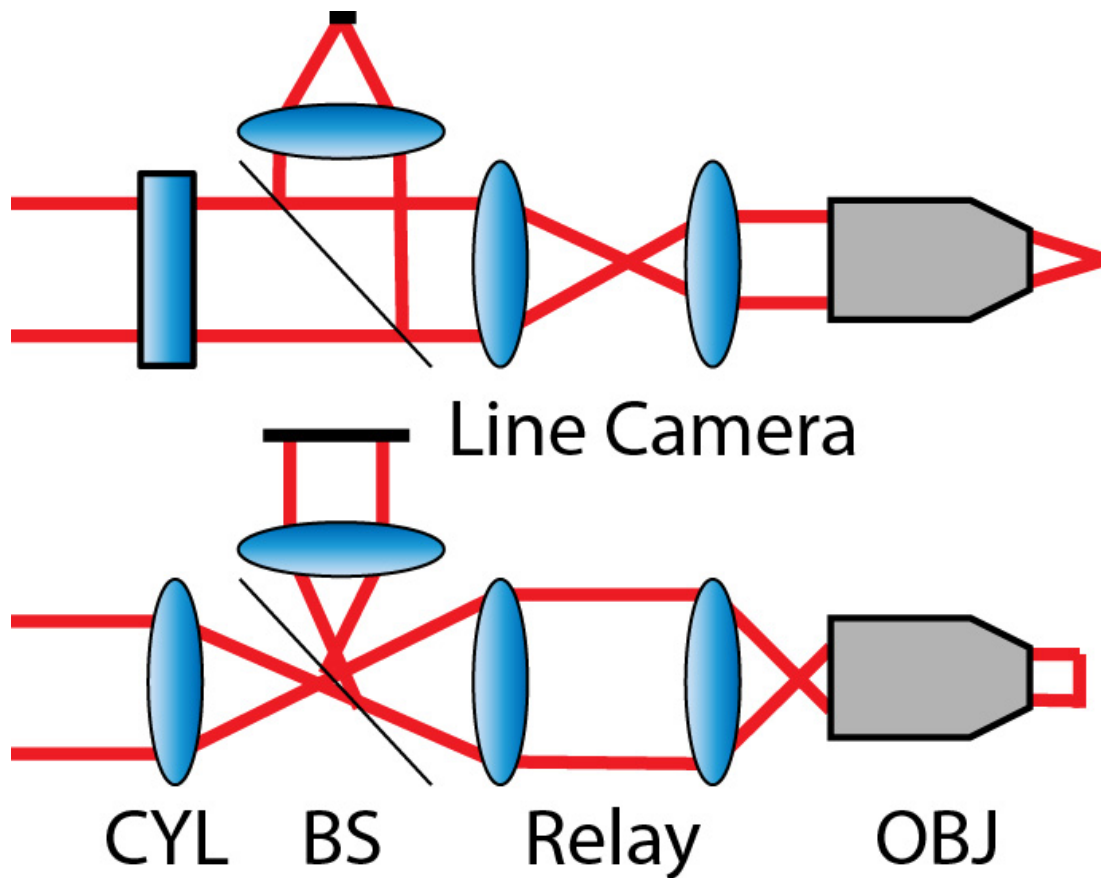
Figure 2.6: Simple line scan confocal schematic. The system is similar to any laser scanning confocal system, where there is a light source, beam splitter, scanning relay, objective, and detector. The graphic on top shows the X-Z plane where a cylindrical lens acts as a piece of glass with no curvature on its surfaces. On the bottom is the system in the Y-Z plane where the cylindrical lens is now acting as a lens with some positive power. The result is a line focus in the sample, which is subsequently imaged onto a linear detector.

over one dimension (at some orientation) to pass, rather than blocking the complete two dimensional Airy disk. As a result, the resolution is slightly worse in the long dimension of the slit. At the same time, the signal level is slightly higher. Since one axis is scanning relatively quickly, this can lend well to techniques which increase the field of view through strip scanning or mosaicing, but typically take an increased time to capture [27, 28].

Another method which can image an entire line at a time is spectrally encoded con-

focal microscopy (SECM) [29]. This technique, based on previous work on wavelength division multiplexing for imaging [30], employs a grating in the imaging system to disperse broadband light over one axis. This effectively encodes position into wavelength. As an advantage over line scanning techniques, the resolution is dependent on the classical pinhole in all dimensions (although spectral resolution of the grating or detection optics could limit resolution in the spectrally encoded dimension). This technique is one of the most developed advanced confocal microscopy techniques. Many advancements on this method have been published including miniaturization [31], high speed imaging [32], and even has a developed in-line dispersion optic called a grism [33, 34] (a combination of grating and prism). SECM has been used in the clinic for esophageal tissue imaging, opthalmoscopy, and breast cancer margining [32, 35, 36].

Dual axis confocal microscopy attempts to improve confocal resolution independently from the NA of the system [37]. This technique can be valuable to miniaturized systems where the NA is restricted due to size (diameter) constraints. The method works by separating the illumination and detection paths into two confocal low NA systems (Fig 2.7). The systems' foci cross in the detection region. This region's size is limited by the overlap of the crossed foci. In single-axis systems ($\theta = 0$), this is also true, which leads to improved resolution (confocal resolution), however, the axial response is still determined by the depth of focus ($DOF \propto 1/NA^2$) which is relatively large for low NA systems. In dual axis systems, the axial response (in the coordinate system of the sample; i.e. z-axis is vertical in Fig 2.7) is partially determined by the lateral full width half maximum, which is much smaller than the depth of field for low NA systems ($FWHM_{lat} \propto 1/NA$). The

resulting resolutions (FWHM) in three dimensions for a low NA optics ($sin(\alpha) \propto \alpha$) is

$$x = \frac{0.37\lambda}{n\alpha cos(\theta)} \tag{2.13}$$

$$y = \frac{0.37\lambda}{n\alpha} \tag{2.14}$$

$$z = \frac{0.37\lambda}{n\alpha sin(\theta)} \tag{2.15}$$

where y is the dimension not in the plane of θ and is just the lateral FWHM of the optics. The technique has been adapted to in vivo imaging methods. Chen et al. achieved video rate imaging at lateral and axial resolutions of 1.2 and 2.2 microns with 0.17 NA lenses [38]. Other groups have miniaturized the design for human imaging and endoscopy [39, 40], including a dual-pupil design (dual axis using two sides of the same objective rather than two objectives) for human skin [41].

All of these techniques attempt to increase speed and better resolution especially for translation to endoscopy (miniaturization). These methods can be combined as well, such as the slit scan SECM [42] and the slit scan dual axis confocal [43]. Other groups focus on miniaturization using MEMs scanners [44, 45] and GRIN optics [46]. This work focuses on the ability to scan in depth, typically ignored by most methods, as benchtop systems will scan depth using a stage. For endoscopes and handheld systems, depth position cannot be held reliably due to a moving patient or shaking hands. Several mechanical axial scanning attempts have been tried [47, 48]. Chromatic confocal microscopy is discussed further in this work as one of the preferred alternate systems for scanning depth. The other preferred method is tunable focus lenses, which are easy to implement. The tunable system and its further development and in vivo results are discussed.
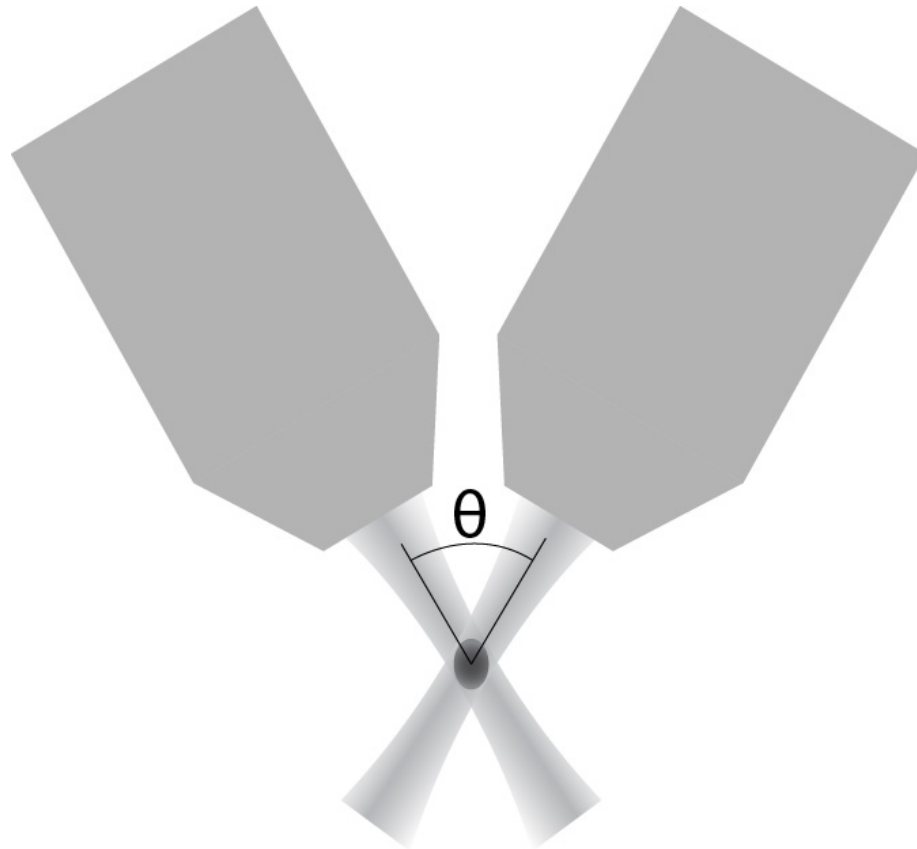
Figure 2.7: Dual axis confocal schematic. One objective belongs to the illumination system and one to the detection system. The systems focuses are confocal and are separated by an angle theta.

3. CHROMATIC CONFOCAL MICROSCOPY*

3.1 Introduction

The work in this section is partially reproduced from [49]. Permission for reproduction in an academic publication is on the authors page of the Optical Society of America website.

Reflectance confocal microscopy (RCM) and optical coherence tomography (OCT) techniques, and combinations thereof, are the primary high resolution volumetric reflectance-based optical imaging modalities being explored for early cancer detection in epithelial tissues. These techniques can provide morphological and architectural information on the tissue, cellular, and sub-cellular scale based on elastic light scattering properties and differences in refractive index [50]. Low-coherence interferometric detection in OCT enables high axial resolution and relatively deep imaging in tissue. However, low numerical aperture (NA) lenses are typically employed, resulting in a lateral resolution insufficient for sub-cellular imaging. In contrast, the high NA objective lenses typically used in RCM enable high lateral and axial resolution for sub-cellular imaging in three dimensions. In comparison to OCT, confocal imaging has shallower penetration in tissue; however, RCM with near infrared (NIR) illumination has sufficient penetration depth for epithelial imaging [51].

RCM frame rates have approached video-rate as a result of methods to increase lateral scanning speed, including fast scanning mirrors, slit-scanning, and spectral encoding of spatial position in the lateral direction [52–54]. Volumetric imaging is typically accomplished by mechanical axial scanning of the imaging optics relative to the sample or the sample relative to the optical system. Mechanical scanning is 1) cumbersome in endoscopic systems, which generally results in larger diameter probes, and 2) time-consuming,

which can lead to severe motion artifacts in reconstruction of volumetric images in living subjects. Hence, a technique to accomplish rapid nonmechanical axial scanning can potentially mitigate image degradation by motion artifact and foster more compact endoscope designs.

Chromatic confocal microscopy is a technique which encodes the focal length, or working distance, into the spectrum of the illumination. Using this technique, we can obtain confocal images at multiple imaging depths without axially scanning. This requires three major modifications to the conventional confocal microscope design. First, we must employ lenses which do not correct for chromatic aberration. Typical confocal systems use well-corrected objective lenses which would minimize the wavelength dependence of focal length. A chromatic confocal microscope takes advantage of longitudinal chromatic aberration which can provide a wide range of focal lengths for a given broadband light source. Second, the light source, which is typically a narrow band laser, should be a broadband light source. A broader range of wavelengths will translate to a broader range of focal lengths, due to the chromatic aberration of the system. Finally, we need spectrally resolved detection. This could be a spectrometer for detecting a broadband source such as a super luminescent diode or supercontinuum light source, or it could be a high bandwidth photodetector for detecting light from a swept-source laser. A conventional confocal microscope integrates all wavelengths from a light source, resulting in a blurring of the axial dimension when there is strong chromatic aberration present. This is why conventional confocal design tries to minimize chromatic aberration and/or minimize the bandwidth of the light source. By employing detection with good spectral resolution, we no longer integrate the focal range created by chromatic aberration, but rather sample the longitudinal dispersion, resulting in collection of multiple confocal sections.

This technique, called chromatic confocal microscopy (CCM), has been used primarily for measurement of optical thickness, topography, and stereoscopy of semiconductor and

19

biological samples [55–57]. Lane et al. [56], presented a promising CCM microendoscope using a GRIN lens; however, images were limited to a resolution target and a microprocessor chip to demonstrate lateral resolution and optical sectioning capability. Shi et al. [58], employed a supercontinuum laser for improved illumination efficiency, but only achieved 7 ţm of focal shift and only images of a transistor were presented. Li et al. implemented wavelength-to-depth encoding for interference microscopy [59]. Early CCM systems were used for profilometry [60] and do not attempt to image in scattering meda. Wavelength to depth encoding has also been used for two photon microscopy [61]. It is worth noting a technique which gives similar results and resolution, broadband axicon OCT [62].

A promising approach is to take advantage of traditionally undesirable chromatic aberrations to generate a longitudinal line focus in the sample that is spectrally encoded in depth [55,56,63]. Spectrally encoding depth enables simultaneous detection of reflectance signal from all points along the line focus, thus enabling significant increases in volumetric image acquisition speed while obviating the need for mechanical axial scanning.

Here we present our effort to design and develop a bulk optic chromatic confocal microscope. Previous CCM systems have exploited the chromatic aberrations in GRIN [56] and Fresnel [55] lenses, both of which suffer from nontrivial spherical aberrations, which limit image quality and resolution in a high-resolution imaging system. In our system, a series of plastic aspherical lenses provide sufficient chromatic shift. With this system, we have obtained the first microstructural images in non-transparent biological tissue using the prototype CCM system, successfully imaging over larger depths than some previous systems while maintaining acceptable resolution for resolving cell morphology.

3.1.1 Methods

The prototype CCM system schematic is shown in Figure 3.1. A broad spectral bandwidth source [Figure 3.2] is created by supercontinuum generation in a photonic crystal

20
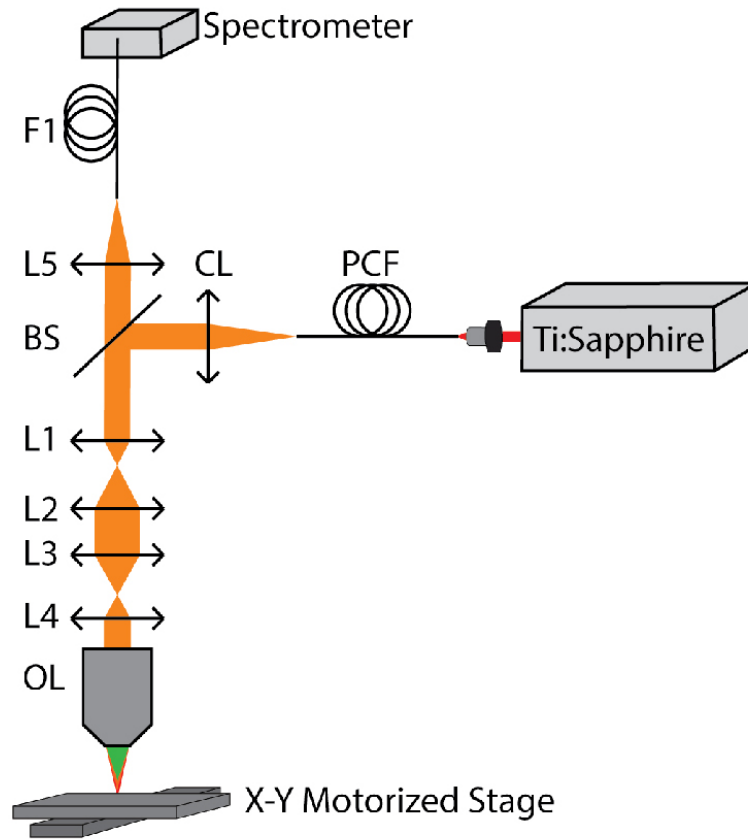
Figure 3.1: Schematic of the chromatic confocal microscope. PCF: photonic crystal fiber supercontinuum source; CL: collimating lens; BS: beam splitter; L1, L2, L3, and L4: aspheric lenses; OL: objective lens; L5: detection lens; F1: detection fiber.

fiber [64], PCF (NL-1.8-845, Crystal Fibre), illuminated with a 140 fs Ti:Sapphire laser (Chameleon, Coherent Inc.) tuned to 800 nm. The maximum pulse energy into the PCF is 50 nJ which provides sufficient power continuously over a broad range of 590-775 nm. After the collimating lens, a 45:55 pellicle beamsplitter (CM1-BP145B2, Thorlabs) reflects the broad bandwidth light into the optical imaging path.

Using ZEMAX software to model the chromatic dispersion, the optical design was optimized for maximum chromatic shift using commercially available lenses. Two sets of relay lenses expand the beam to fill the back aperture of the objective lens and con-
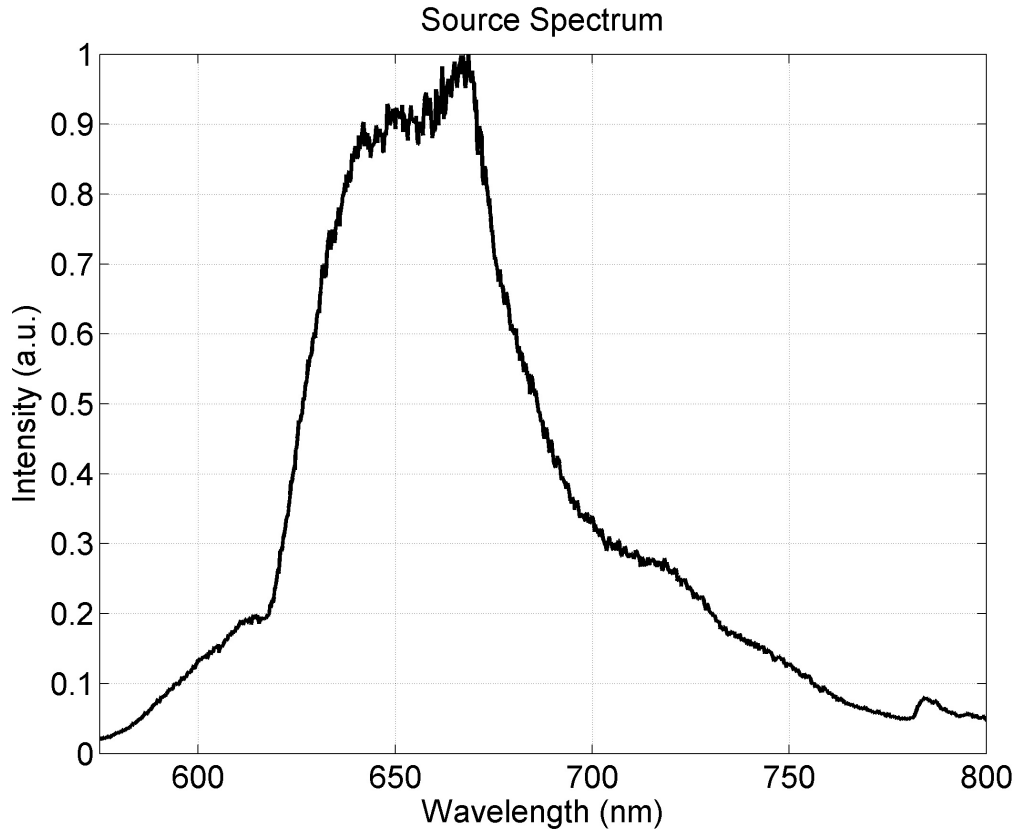
Figure 3.2: Reference spectrum of the supercontinuum source measured by the spectrometer through the optical system.

tribute to the chromatic aberration. The two relays consist of four aspheric lenses, L1 (f = 8 mm; A240TM-B, Thorlabs), L2 (f = 17.5 mm; NT66-020, Edmund Optics), L3 (f = 40 mm; NT66-024, Edmund Optics), and L4 (f = 20 mm; NT66-021, Edmund Optics). Aspheres are well corrected for spherical aberration, but exhibit strong longitudinal chromatic aberration. The dispersion of the lenses is characterized by the Abbe number of the lens material, where lower Abbe numbers translate to stronger dispersion. L1 is made from S-LAL13 glass, Abbe number 53.2, and L2-L4 are made from Zeonex E48R plastic, Abbe number 51.66. A well-corrected, water immersion 40Œ 0.8 NA lens (CFI Apo 40XW NIR, Nikon) is used as the objective. This lens should not add significant

aberrations (desired or otherwise) to the system. Each wavelength is focused to a different relative position in the object determined by the dispersion and magnification of the preceding lenses, illustrated in Figure 3.3. Based on the ZEMAX model, the chromatic focal shift, z in Figure 3.3, for the 590-775 nm wavelength range, at the beam focus between L1 and L2 is 98 ţm. After passing through L2 and L3, z at the beam focus between L3 and L4 is 1.939 mm. Although the ZEMAX lens data is not available for the Nikon objective lens, we model the longitudinal magnification of the objective using a simple lens with the same focal length, 5 mm, and then, assuming no chromatic aberration in the objective, remove the chromatic shift associated with that simple lens to estimate the chromatic focal shift of the total lens system. We estimate approximately 159 ţm chromatic focal shift in the object for the 590-775 nm wavelength range.

Since the lens system obeys the principle of reversibility, the reflectance signal from each focal point in the object is recombined into a single collimated beam before the beam splitter. The detection lens, L5 (f = 100 mm; AC254-100-A-ML, Thorlabs), couples the light into the detection fiber F1 (P2-2000-PCSMA-1, Thorlabs), with a core diameter of 11 ś 1 ţm. The detection lens and fiber are designed to be a fairly typical confocal spatial filter by making the spot size and fiber core diameter approximately equal. A commercial spectrometer (USB4000, Ocean Optics) captures the spectrum of the reflectance signal directly from the detection fiber, which corresponds to an A-scan, or axial depth scan. Three dimensional volumetric images are acquired by two dimensional raster scanning of the sample using a pair of X-Y mounted motorized stages (T-LSM, Zaber, Inc). The collected volume was normalized to the reference spectrum. To reduce the file size, the spectral data was resampled from 0.19 nm/pixel to 0.95 nm/pixel by window averaging every 5 samples in wavelength; this results in an average pixel size of 1 ţm in the axial direction. The resolution is not affected by the reduction of the sample size since the optical resolution is oversampled in the spectrometer.
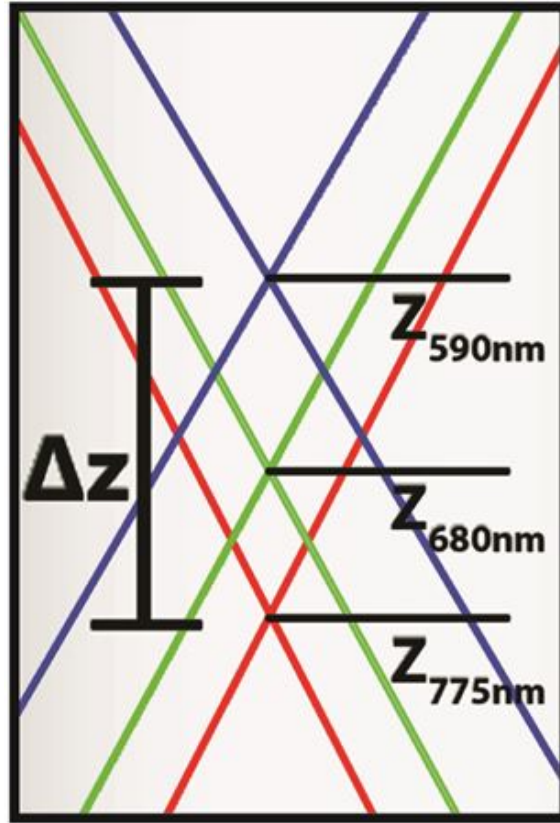
Figure 3.3: ZEMAX ray trace at the focal plane.

In CCM, the range of wavelengths results in a number of factors affecting the wavelength-dependent resolution, including objective lens NA, focused spot size on the fiber core, fiber V parameter, and spectral resolution of the spectrometer. Additionally, changes in the fiber V parameter affect mode excitation and fiber coupling. The axial optical point spread function in the sample space $[oPSF(\lambda)]$ of CCMs has been modeled for finite pinhole sizes and for single-mode fibers as detection apertures [65, 66]. Based on the range of fiber V parameter over the bandwidth, we estimate between 14-26 modes are excited in the fiber; therefore, we use the finite pinhole model.

The theoretical axial point spread function of a CCM is calculated by modeling the

detected intensity [23],

$$I(u) = \int_0^{v_p} \left| \int_0^1 P(\rho) \exp(\tfrac{1}{2} j u \rho^2) J_0(v\rho) \rho d\rho \right|^2 v dv \qquad (3.1)$$

as a function of the normalized optical units,

$$u = \frac{2\pi}{\lambda} \frac{NA^2}{n} z \qquad (3.2)$$

$$v = \frac{2\pi}{\lambda} NAr \qquad (3.3)$$

where $P(\rho)$ is the pupil function of the objective, v_p is the pinhole radius in normalized units, λ is wavelength, NA is the objective numerical aperture, n is the refractive index of the immersion medium, and z and r are the real axial and radial optical coordinates, respectively. The CCM detector is a spectrometer which has a resolution in part defined by the optical point spread function on the line detector, $sPSF(\lambda)$. Since the axial space is encoded in the spectral domain, the $sPSF$ of the spectrometer contributes to the width of the measured axial point spread function $PSF(\lambda)$. Assuming a perfect detector, the $PSF(\lambda)$ measured at the spectrometer is therefore the convolution of the $oPSF(\lambda)$ and the $sPSF(\lambda)$ determined by the spectrometers optics, i.e.

$$PSF(\lambda) = oPSF(\lambda) \otimes sPSF(\lambda) \qquad (3.4)$$

where $\otimes$ denotes the convolution operator.

As wavelength increases, the normalized pinhole, v_p, decreases and optical sectioning is enhanced (i.e. smaller $oPSF$), since the spot in the detector plane grows larger compared to the fiber core. In opposition, longer wavelengths yield a larger $oPSF$ in the object (sample) space. In the wavelength range where the spot size is smaller than the

pinhole, the FWHM plot as a function of wavelength exhibits a low amplitude oscillating pattern [65]. The slight decrease in NA increases the $oPSF$ for longer wavelengths; however, the effect is negligible for small focal shifts.

Using the design NA of the objective (0.8 in water) to estimate the axial resolution of the CCM, the resulting theoretical axial full-width half-maximum (FWHM) of the $oPSF$ varies from 1.13-1.43 µm over the 590-775 nm wavelength range, respectively. The $sPSF$ is approximated by a Gaussian function with a FWHM (given from specifications) of 1.5 nm. The oPSF is converted to wavelength using the measured dispersion curve (Equ. 3.5), convoluted with the $sPSF$, and the resulting PSF is converted back to axial coordinates using Equ. 3.5. The convolution of the $oPSF$ with the $sPSF$ yields a theoretical FWHM of the total PSF ranging from 2.17-1.57 µm over the 590-775 nm range, respectively. The spreading effect from the $sPSF$ affects the shorter wavelengths more strongly since the dispersion is much stronger in this range bringing the optical PSF closer to the spectral resolution limit.

The axial resolution as a function of wavelength was experimentally measured by translating a mirror through the foci of the CCM system and recording spectra as a function of axial position of the mirror. This data also served to measure chromatic shift over the full spectrum of the system and was used to normalize subsequent spectra.

To evaluate imaging of non-transparent tissue, a thick tissue sample of porcine buccal mucosa was imaged ex vivo. The tissue was immersed in acetic acid for 30 seconds to enhance backscattering from cell nuclei [67]. 500x500x157 µm^3 volumes were captured using a 1 µm lateral sampling interval and 7 ms integration time. The lateral direction is intentionally undersampled to improve speed and reduce memory requirements. Images were compared to traditional reflectance confocal images acquired with a Lucid Vivascope 2500 confocal microscope with 830 nm illumination wavelength, 0.9 NA, and <2.0 µm lateral and <5.0 µm axial resolution.

3.1.2 Results
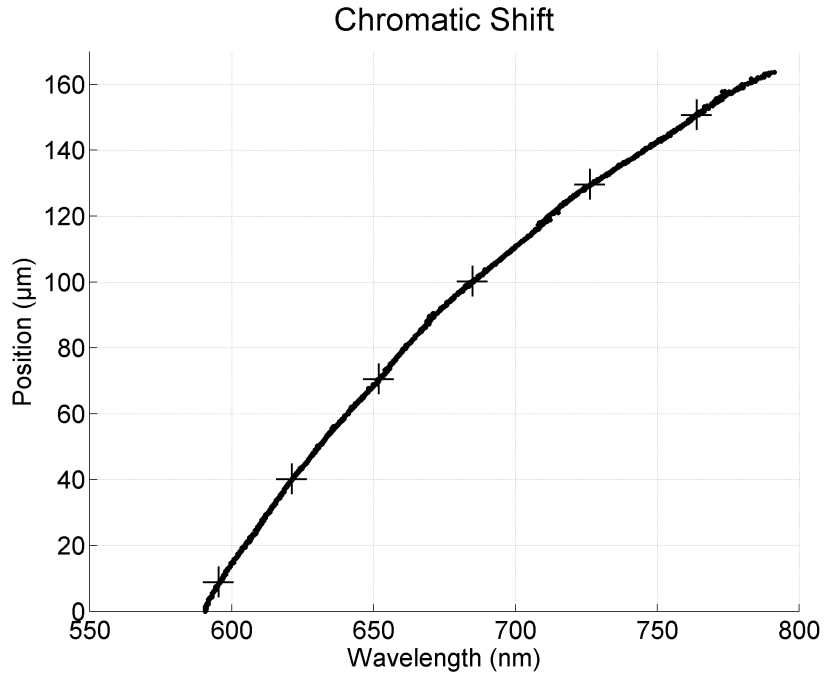
Figure 3.4: The chromatic shift shows the relative focus for each wavelength. The total shift is 157 țm over a 185 nm range.

In order to evaluate the performance of the imaging system, we translated a mirror through the foci and recorded the spectra as a function of axial position of the mirror. The chromatic focal shift [Fig. 3.4] is plotted by finding the peak intensity wavelength for each axial position. Over the 590-775 nm wavelength range, the foci span a depth range of 157 țm, which corresponds well with our optical model. A quadratic fit ($R^2 = 0.999$) to the experimental measurements yielded a calibration curve to convert wavelength in țm to relative axial position in țm,

$$z(\lambda) = -2213\lambda^2 + 3850\lambda - 1498 \tag{3.5}$$

27

where $z = 0$ ţm represents the shortest focal position, at $\lambda \approx 590$ nm. The signal versus mirror position can be plotted to show the axial PSF for each wavelength. Fig. 3.5 shows the axial PSF for four wavelengths. Over the entire wavelength range of 590-775 nm, the average measured FWHM axial resolution was 3.1 ţm; however, the value varies irregularly between 2.0 to 4.4 ţm due to the multifarious wavelength dependence of axial resolution discussed in the Methods. The lateral resolution was obtained by imaging a Ronchi grating with the center wavelength and measuring the edge resolution (10%-90%). The pixel size of the grating image was set to oversample a Ronchi edge at 0.17 ţm/pixel. The measured lateral resolution is 0.7 ţm, whereas the theoretical lateral resolution, based on the Rayleigh criterion, is 0.5 ţm.
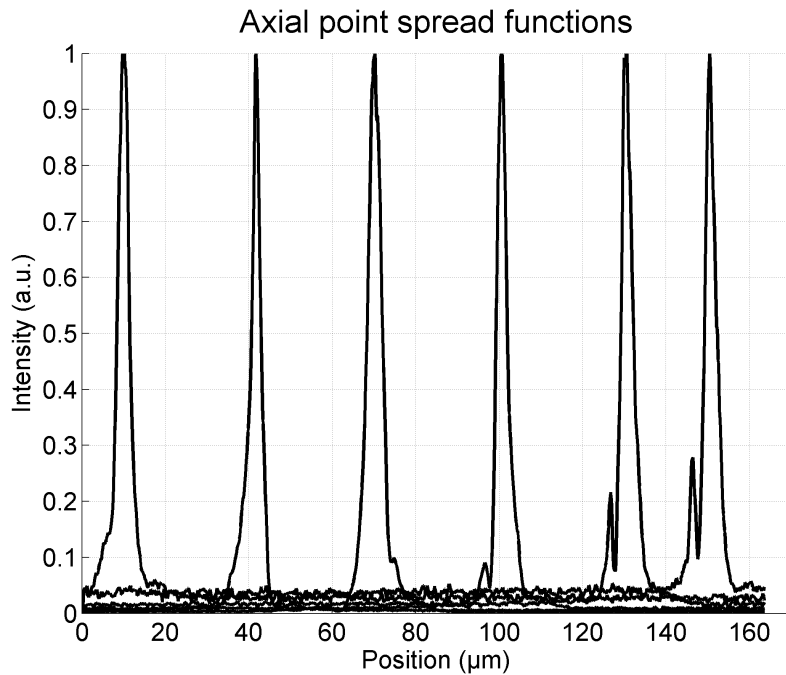
Figure 3.5: Four axial PSFs are shown at 10, 50, 90, and 130 ţm depth at wavelengths of 595, 635, 675, and 725 nm, respectively. The peak of each PSF corresponds to a single wavelength which is converted to relative depth using a calibration curve. The FWHM from left to right is 3.2, 2.9, 3.1, and 3.1 microns

The porcine buccal mucosa volumes demonstrate the ability to resolve cellular features. An image stack from a shallow depth in the tissue (0-150 ţm) is shown from the CCM volume [Fig. 3.6]. This can be compared with an image captured with the commercial confocal microscope of a similar region [Fig. 3.7]. The differences in contrast and appearance can be due to variations in the tissue; however, the image quality is overall similar. Fig. 3.6 is a video captured from a CCM volume deeper in the tissue (100-250 ţm). Basal cell nuclei, which are more crowded than superficial cell nuclei, can be seen in the video. Since imaging speed is slow in this CCM system, finding the absolute depth in tissue at which to begin imaging was done by acquiring A-scans in time (M-scans) then adjusting the stage so that signal begins at the shallowest point in the depth scan. This method was unreliable and, as a consequence, imaging required multiple trials.
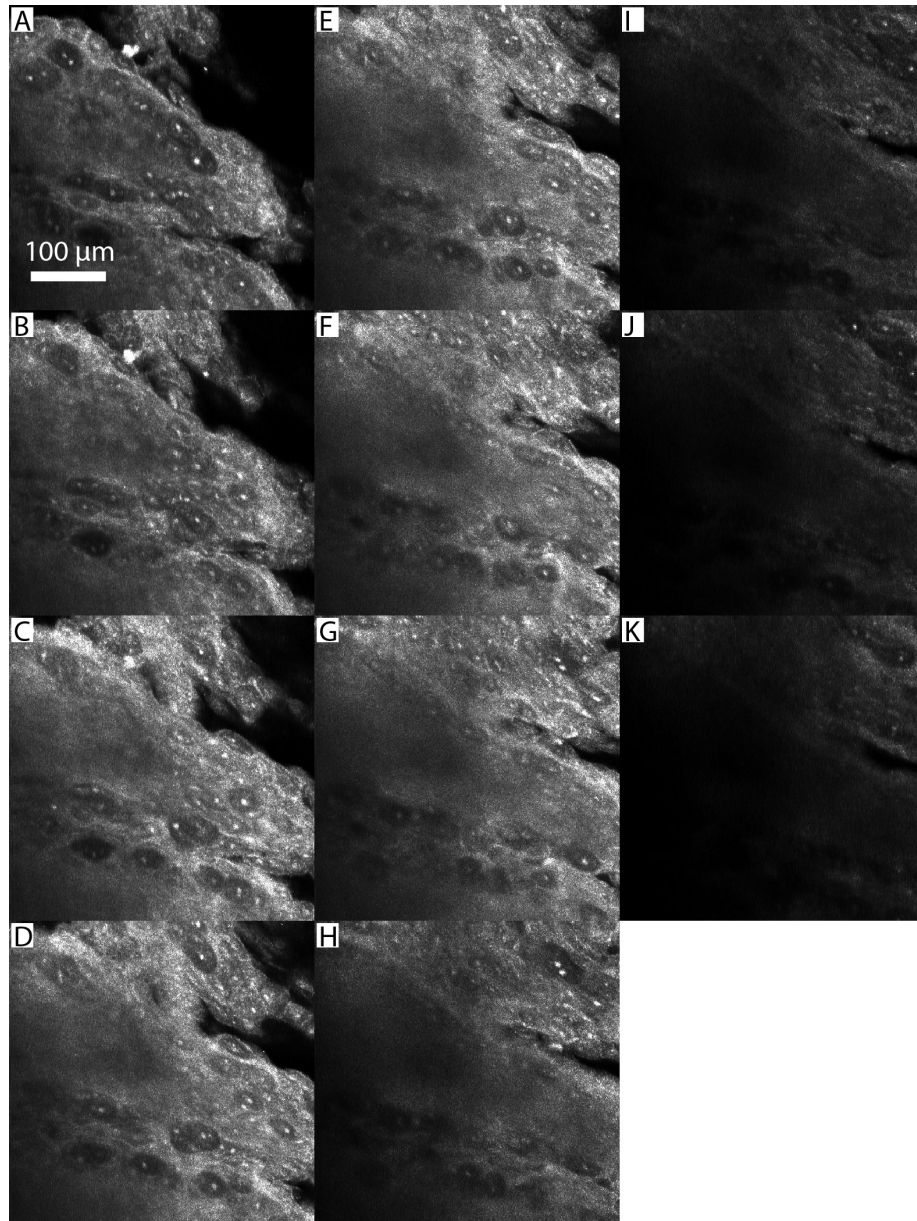
Figure 3.6: Subset of shallow CCM stack in 10 ţm increments (alphabetical order). Several distinct layers in the upper epithelium can be seen. Some cells are thicker than 10 ţm and can be seen in multiple images.
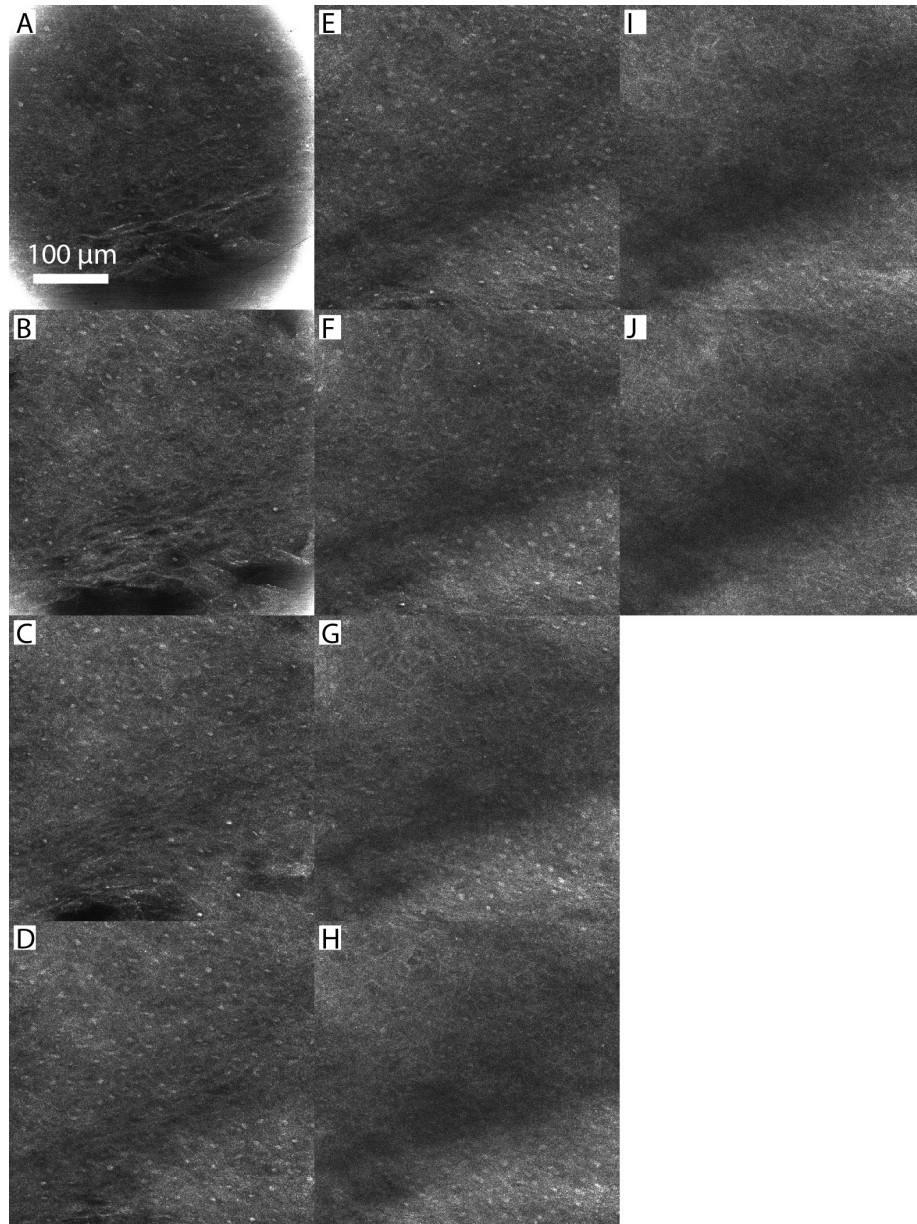
Figure 3.7: Image stack from commercial benchtop confocal. Images are in 10 ṭm increments.

3.1.3 Discussion

As noted above [see Fig. 3.5] the measured PSF has a FWHM of 3.1 m at 650 nm. Without considering the spectrometer optics the axial FWHM at 650 nm is 1.21 ṭm; how-

ever, the limited spectral resolution of our spectrometer yields a 1.90 ţm theoretical axial FWHM. This result is in better agreement with our measurement and demonstrates the influence of spectral resolution on the axial resolution in our system. From an inspection of the PSFs in Fig. 3.5 it is clear from the asymmetry that there is uncorrected aberration in the microscope and/or spectrometer optics which is the likely source of most of the residual difference between measured and calculated resolution. The shoulders on the PSFs can also contribute to reduced contrast in the image.

The porcine buccal mucosa volumes presented here demonstrate the capability of the described chromatic confocal microscope to image epithelial tissue with sufficient spatial resolution and chromatic shift to resolve cell nuclei over multiple cell layers. The cellular features resolvable in single-depth CCM images in Fig. 3.6 obtained from three dimensional data sets are comparable to those obtained by a commercial reflectance confocal microscope that uses traditional single-depth imaging without chromatic aberration [Fig. 3.7]. While traditional confocal microscopes require physical translation of the sample or objective lens to acquire data in depth, the CCM captures confocal reflectance data over the 157 ţm depth range of the chromatic shift in a single shot. The spectral encoding of depth is decoded using a spectrometer. Although relatively simple changes are made to a reflectance confocal microscope to achieve depth encoding, the same changes cannot be applied to one-photon fluorescence confocal microscopes due to the Stokes shift of the fluorescence emission. The emission spectra of fluorophores are independent of excitation wavelength; therefore, all depth-to-wavelength codification is lost and emission light would be spatially filtered out by the confocal pinhole. In contrast, chromatic axial scanning has been applied to transmission second harmonic imaging and demonstrated over an 8 ţm axial scan range using 8 nm second harmonic wavelength range [68]. Additionally, one-photon fluorescence imaging has been achieved using spectral encoded imaging by correlating temporal signal with a wavelength-swept source [69]; however, this system is

32

not confocal and therefore not optimized for thick turbid samples. Ideally, the chromatic focal shift at the sample would span up to 300 ţm, which would cover the full epithelium and the full range of imaging depth with NIR RCM in most epithelial tissues. For shorter wavelengths, penetration depth is limited; however, dispersion from refracting optics focuses shorter wavelengths to shallower depths. Extending the spectral range of our source further into the NIR wavelengths will reduce scattering and improve penetration depth but will not yield significant chromatic focal shift due to flattening of the dispersion curve. The effect can be seen at longer wavelengths in the chromatic shift curve in Fig. 3.4. If a custom lens is designed for this application, lens material with stronger dispersion in the NIR range could provide the necessary chromatic shift. Using hyperchromat theory in the lens design [70] could also increase chromatic dispersion as well as linearize the focal shift. Hyperchromats are not currently used due to limited selection of commercially available sizes and focal lengths. Magnification is an important factor when optimizing chromatic shift. Typically the objective demagnifies a chromatic shift from back aperture to the focal plane. If the magnification from source to sample is increased (less demagnification), the chromatic shift will be greater. However, the beam size in the Fourier plane of the objective is reduced, decreasing numerical aperture and therefore diminishing resolution. Designing a custom objective would allow better control over optimization of numerical aperture and magnification.

3.2 Design Considerations

Increasing dispersion to gain chromatic shift also places more demands on the detection spectrometer. The axial point spread function (PSF) remains constant in space; hence an increase in dispersion results in a decrease in the spectral width of the PSF and a concomitant increase in the required spectral resolution. This is evident in the performance of our current system and is considered in our theoretical axial FWHM calculations above.

Going forward, the development of a custom spectrometer with optimized resolution for the designed chromatic dispersion with well corrected optics will be key to realizing the full potential of the CCM system.

An alternative way to design the CCM is to use diffractive optics such as circular gratings [71] or a Fresnel lens (grating period proportional to radius).

In principle, the CCM technique can enable high speed volumetric imaging; however, the current prototype is limited by the translation stages used for x,y scanning and the slow read-out time (7.5 ms) and optical inefficiency of the commercial spectrometer detector. Currently, a 500x500 ţm2 x,y scan at 1 ţm sampling interval can take up to 30 minutes. Slow scanning speed can readily be addressed by incorporating more traditional galvo mirror based x,y scanning. Likewise, a custom built efficient spectrometer incorporating a high-speed line scan camera with the appropriate spectral resolution would address the limitations of our current spectrometer.

We can estimate the ultimate imaging speed of our CCM system by making a few reasonable assumptions about our system and sample from the perspective of the signal to noise ratio of a confocal microscope [72]. We will define the limit of detection as the power at which the signal to noise ratio (SNR) is equal to one. The power that reaches the detector is determined by the losses in the system, the power incident on the sample, and the reflectivity of the sample. The losses in the system can be estimated based on our current CCM system and replacing the spectrometer with a high efficiency design; the loss from the optics and pinhole results in approximately 4.5% transmission, so a spectrometer with a grating efficiency of 80% would bring the total efficiency to 3.5%. The maximum power incident on the sample is determined by the ANSI maximum permissible exposure (MPE) [73]. The MPE is a function of the dwell time on the sample or the number of pixels times the sum of the integration and read-out times. The maximum SNR can then

34

be defined as (modified from [74]),

$$SNR = \frac{\frac{\text{MPE}}{p_x E} QFR}{\left(\frac{MPE}{p_x E} QFR + n_d^2 + n_r^2 \right)^{1/2}} \tag{3.6}$$

where Q is quantum efficiency, F is the efficiency of the system, R is the reflectivity of the sample, p_x is the number of pixels in an image, E is the energy of a photon, n_d is the dark noise, n_r is the readout noise, and

$$\text{MPE} = 1.1A(p_x t_p)^{0.25} \text{ [J]} \tag{3.7}$$

where A is the area of the limiting aperture (3.5mm diameter for skin), and t_p is integration time. Equ. 3.7 assumes we will not image an area larger than the limiting aperture and that there is only one exposure, repeated exposures would have a lower MPE. At low light levels and low integration times, readout noise is the main source of noise; therefore, the SNR can be simplified to

$$SNR = \text{MPE} \frac{QFR}{p_x E n_r} \tag{3.8}$$

We can then solve for R assuming a limit of detection of $SNR = 1$ and define this quantity as the noise equivalent reflectivity (NER). If we assume a commercial linear CCD array (E2V, AVIIVA EM4) with 210 kHz line rate, a quantum efficiency of 0.8, and a readout noise of 50 e- RMS, we can calculate the NER. Given an image size of 500x500 px^2 and 600 nm wavelength light, the NER would be 5x10^{-7}. Cell nuclei have a reflectivity between 10^{-4}-10^{-6} [74], well above the NER. When the reflectivity is much higher than the NER, shot noise becomes important and Equ. 3.6 is more appropriate. Under these conditions we could collect a 500x500 px^2 volume in 1.2s.

3.3   Future Work

In summary, we have developed a CCM that utilizes a supercontinuum source, incorporates aspheric lenses for chromatic dispersion, and utilizes spectroscopic detection to simultaneously capture reflectance confocal signal over a 157 m axial range in tissue. Volumetric images of cells in pig oral epithelium are presented. Although the current imaging speed is slow, straightforward improvements in the experimental design can decrease imaging time to less than 2 seconds per volume. The ability to capture volumetric reflectance confocal imaging data without mechanical axial scanning is attractive for clinical endoscopy applications due to the reduced complexity in the endoscope and a reduced susceptibility to motion artifact. Most current confocal endoscope designs either only collect 2-D images or utilize relatively slow axial scanning mechanisms. CCM can be combined with line scanning for improved speed and simpler design [75].

4. CONFOCAL MICROSCOPY WITH
A TUNABLE LENS

4.1 Introduction

Lesions in the oral epithelium have characteristic morphologies which can be classified through histopathology as malignant, precancerous, or benign. Our handheld confocal endoscope is designed to acquire images of oral epithelium in vivo so that the most ideal biopsy site(s) can be chosen for an accurate diagnosis. A histology section from the oral epithelium is typically a longitudinal cut so that morphology can be analyzed through the depth of the tissue. Traditional confocal microscopes, producing lateral images, require scanning a stage holding the specimen to image multiple depths, which cannot easily be done in vivo. In vivo depth scanning has been attempted by several techniques including mechanical scanning [47,48], depth-to-wavelength encoding [49], and tunable focal length elements [76, 77]. Our system employs an electrically tunable lens (ETL) to change the focus of the endoscope while it is in contact with tissue. The ETL was chosen because it does not require any large mechanical motion to tune while it still offers a very large focal length range.

The original design of our confocal endoscope collected images in vivo [78] and utilized a separate illumination and detection pathway with a confocal pinhole; however, the pinhole needed to be continually aligned after repeated handheld use, as resolution would degrade due to misalignment. The design was also cumbersome which caused operator hand fatigue and led to motion artifact. Practical design is needed for imaging oral epithelium with confocal microscopy to determine efficacy of optical biopsy results [3], which includes design for reliability and ergonomics. We have improved the design by replacing the collection path with a double clad fiber coupler. The double clad fiber delivers light

through the core to the probe and collects the reflectance signal through the inner cladding in a partially coherent detection scheme. Fiber alignment is no longer necessary as the faces of the core and inner cladding inherently lie in the same plane. Another improvement is the modification of the custom objective lens which changes the working distance range. The original design sacrificed image quality at short working distances for a large range. A coverslip cemented to the lens tip provides the ability to shift the short working distances to a range with better image quality in exchange for reducing the range by 100 microns. The modification is an inexpensive solution to improve results immediately. Additionally, we have replaced the housing with a new 3D printed housing which reduced the weight by 1.14 pounds and reduced the size by 10% in each direction. These changes have led to more consistent results which is essential for determining the microscopes ability to diagnose pre-malignant lesions.

4.2 Methods

4.2.1 Overview

The microscope consists of a handheld rigid probe containing the optics and scanning unit, and an equipment cart containing the laser, detector, and control and acquisition electronics. The probe is tethered to the cart with a black flexible corrugated wire loom which routes the optical fiber and the control wires of the mirrors and ETL. Light is delivered and collected through a double-clad fiber coupler.

The probe (Schematic in Figure 4.1) contains a fiber collimator followed by an ETL (Optotune, EL-6-18). The ETL is a deformable polymer surface in a lens package which allows tunability of the divergence of the beam, and ultimately the working distance of the system. After the ETL, a 2D scanning unit scans the beam (Cambridge Technology, CRS 8 KHz resonant scanner and 6200H galvanometer scanner). The resonant scanning mirror scans the beam in the X direction with a sinusoidal scan at a frequency of 7.91 kHz
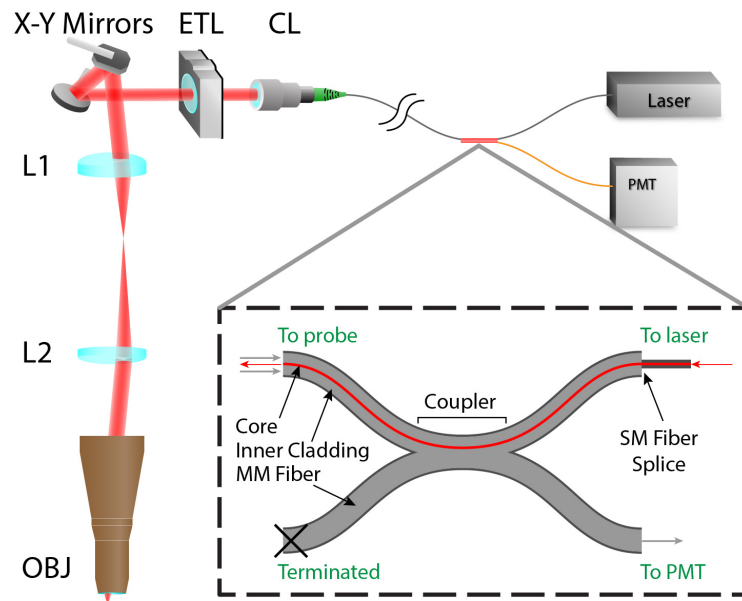
Figure 4.1: Schematic of RCM system. The probe components are the collimator lens (CL), electrically tunable lens (ETL), X-Y scanning mirrors, 25 mm and 50 mm relay lenses (L1 and L2, respectively), and custom objective (OBJ). (inset) Double-clad fiber coupler. The laser is coupled to the input by single mode fiber. The double-clad fiber illuminates through the single mode core and collects in the inner cladding. The collected light is coupled to the multi mode fiber and directed at a PMT sensor.

and the galvanometer scanning mirror scans the beam in the Y direction with a smoothed sawtooth scan at a frequency of 6.6 Hz, the frame rate. The beam is relayed to the objective lens with a 2X relay made from two custom achromatic doublets manufactured by Optics Technology Inc., which are designed to balance aberration for off axis beams. The lens prescription for the relay and objective is in Appendix **??**. A view of the inside of the probe was rendered in Solidworks and is seen in Figure 4.2. The scan angles of the mirrors are set so the field of view is 850ţm. The original custom 0.7 NA 5mm focal length water dipping objective [78] was modified by cementing a #1.5 coverslip to the tip of the lens. The modified objective focuses the beam at a nominal working distance of 180 microns.

The working distance can be adjusted between 0μm and 265μm by supplying a current between 135mA and 0mA respectively to the ETL. All the components are mounted on a machined aluminum body and housed by a 3D printed ABS plastic shell. The shell has been washed with acetone to temporarily dissolve the surface allowing it to smooth for a nicer appearance, better grip, and easy cleaning. The final probe is pictured in Figure 4.3. The power and control wires for the mirrors, ETL, and double clad fiber are routed through a single corrugated wire loom to the base cart.
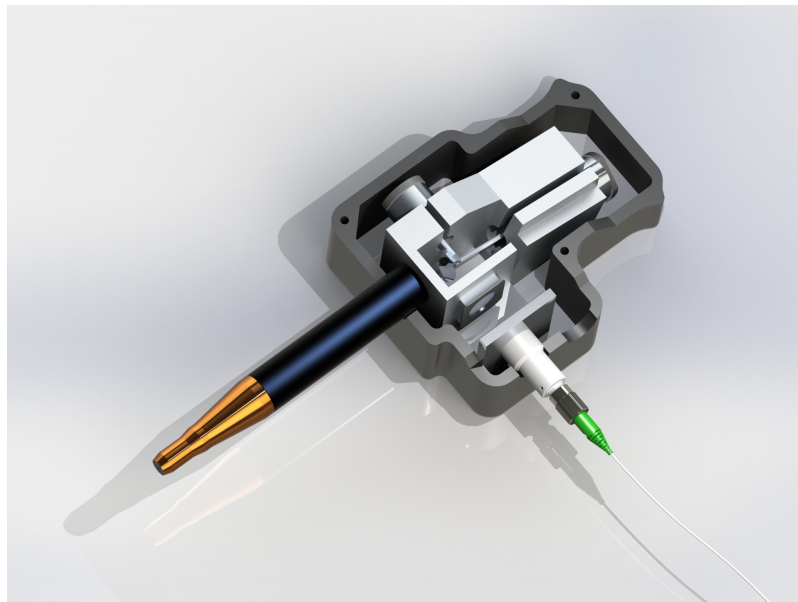
Figure 4.2: Solidworks rendering of inside of probe.

The image quality near the 0μm working distance is poorer than at the nominal working distance due to aberration from the ETL and relay lenses and a lower effective NA due to beam convergence causing underfilling of the objective. These effects are reduced by the working distance modification to the objective lens. The maximum depth is now shorter compared to the design using the original objective, however, penetration depth in the oral

Figure 4.3: Photo of final probe.

epithelium is typically under 200 microns, less than even the new focal range. The depth of an image inside the tissue can be approximated using a calibration curve to convert ETL current to depth in microns. The calibration is obtained by decreasing the ETL current incrementally while using a mirror mounted on a linear stage (Zaber Technologies) to determine the focus (when backreflected light is at maximum).

4.2.2 Lens Design

The design of the original system included two off the shelf relay lenses and a custom objective. The custom objective (Appendix A.2) was designed for a nominal working distance of 300 ţm. Performance at other working distances was taken for granted, as test objectives did not present significant quality loss. However, it can be seen in a closer analysis of the modulation transfer function (MTF) that the performance will significantly more poor at shorter working distances. Additionally, the use of off the shelf relay lenses will not guarantee good performance as they are optimized for infinite conjugates. As the ETL is tuned, the light is either diverging or converging at the surfaces of the relay lenses,

which will add aberration. Figure 4.4 A and B show the MTF for the original system. The figures on the left are at 0 ʈm field and the figures on the right are at 175 ʈm field. "A" is the old system at the nominal working distance. The objective should be diffraction limited here, however, the relay lenses add this aberration which is very significant at even a modest field of view. Moving to a shorter working distance shows more severe aberration as well as a lower diffraction limit due to the smaller aperture (from converging beam). The new system includes a custom design relay (Appendix A.2) and a coverslip to offset the working distance. The relay was optimized for use with the coverslip and at several working distances. The coverslip simply acts as an offset so that the beam will not need to converge so strongly for very short working distances. In Figure 4.4 C the MTF at the nominal working distance of the new system is shown. We can compare it to "A", where the working distance is longer but the state of the ETL is the same (i.e. no convergence at objective). Here the performance is slightly worse at 0 ʈm field due to the use of the coverslip. The coverslip is not optimized optically and only acts as an offset, so we should expect more aberration for any given ETL position/state. However, the 175 ʈm field is significantly better, owing to the custom relay lenses. We can also compare "C" to "B", where the working distances are the same, but the ETL position is set to converge in the original design. This is important because this compares what the image quality will be at a specific point in the sample. Here we have the same loss of quality at 0 ʈm, but the improvement is even greater at 175 ʈm.

The quality is enhanced at other working distances as well. In Figure 4.4, the working distance, 175 ʈm, is considered long relative to the thickness of the human oral epithelium. Figures 4.5 and 4.6 show the MTFs of the original system in "A" and the new system in "B". Figure 4.5 shows the MTF at a working distance of 10 ʈm, which is considered short. The improvement at 0 ʈm field is mostly due to the higher effective NA gained from using a less converging ETL state. The 175 ʈm field is improved from both the effects of higher

effective NA and aberration correction from the custom relay lenses. Figure 4.6 shows the MTF at a working distance of 65 ţm, which is considered medium working distance. The same improvement is seen, where we have a higher effective NA and better aberration correction in the higher fields.

The lenses were manufactured by Optics Technology Inc. Before the lenses were implemented into the system, a simple workaround was used in place. A coverslip was glued to a removable 3D printed cap which could be quickly used to place the offset coverslip over the objective. The axial response and lateral resolution was measured with this intermediate system at multiple working distances. The measurement was repeated when the lenses arrived. The results are reported in the results section.

4.2.3 ETL

The ETL is placed before the scanning mirrors so the chief rays are not altered when tuning the focus. For an ideal telecentric imaging relay, this means that magnification is constant over the axial scanning range. Another valid position for the ETL is in the back focal plane of the objective, where all chief rays pass through the center of the aperture. However the ETL is large and would be too obstructive for an intraoral probe. Since the ETL is in front of the relay lens (Figure 4.1), the available focal range will be reduced due to longitudinal magnification of the relay and objective lenses. Even so, the focal range for this configuration is acceptable. An additional benefit to placing the ETL before the scanning module is that aberrations due to off axis rays entering the ETL are avoided.

4.2.4 Double-clad Fiber Coupler

The coupler is a double-clad fiber with the inner cladding coupled to a multi-mode fiber. The 811 nm DPSS laser (Crystalaser) is coupled to a single mode fiber spliced to the core of the double-clad fiber so the laser is only coupled into the core of the double-clad fiber. The illumination light is delivered through the core to the probe then the back
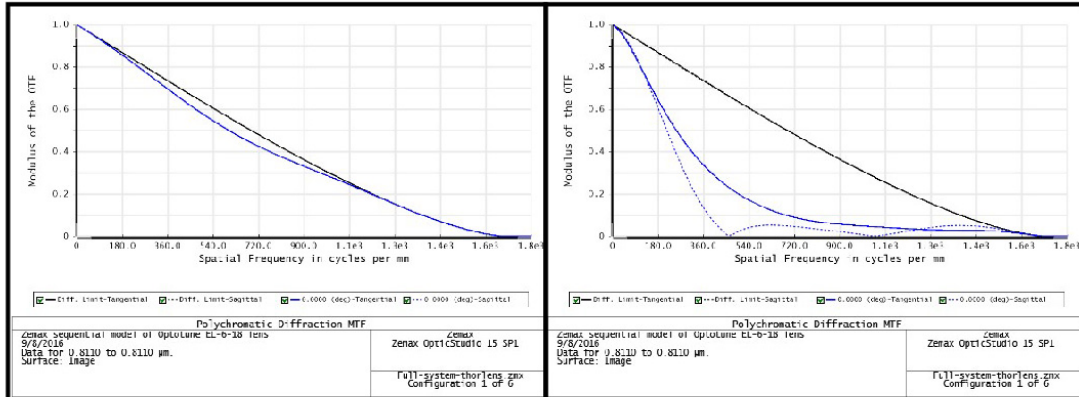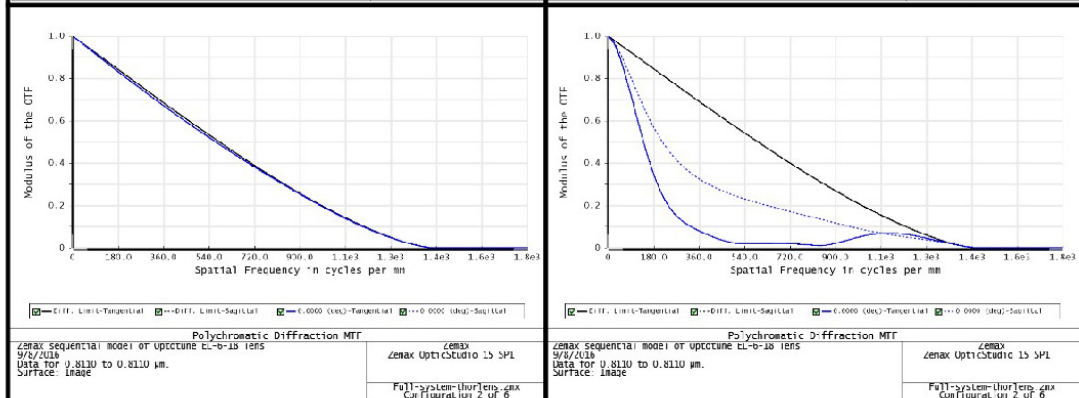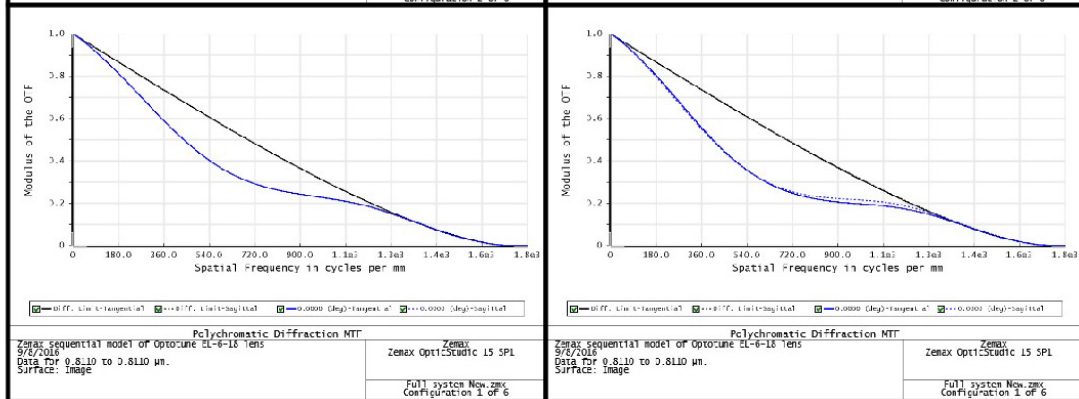
Figure 4.4: Modulation transfer functions of system. (left) MTFs at 0 ţm field. (right) MTFs at 175 ţm field. (A) Original system at nominal working distance - 300 ţm. (B) Original system at 175 ţm working distance. (C) New system at nominal working distance - 175 ţm
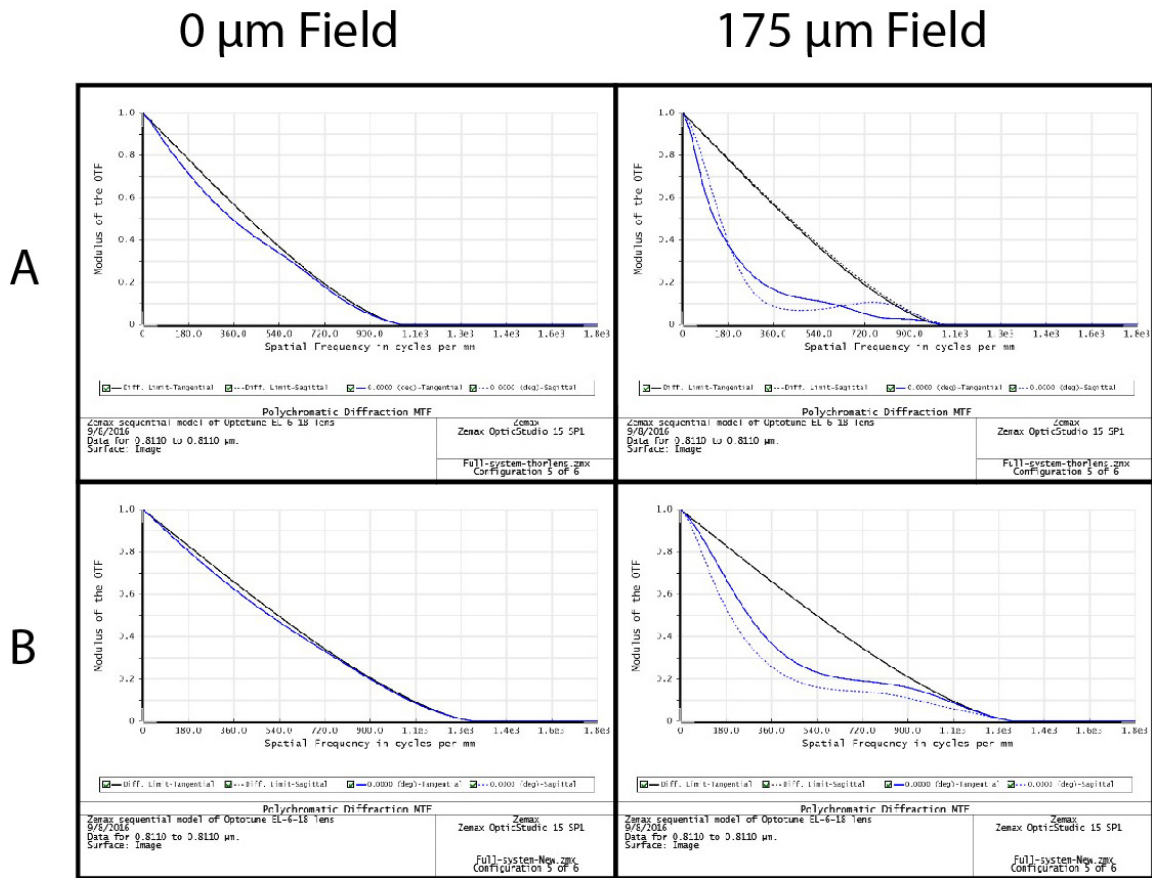
Figure 4.5: Modulation transfer functions of system. (left) MTFs at 0 ţm field. (right) MTFs at 175 ţm field. (A) Original system at 10 ţm working distance. (B) New system at 10 ţm working distance.
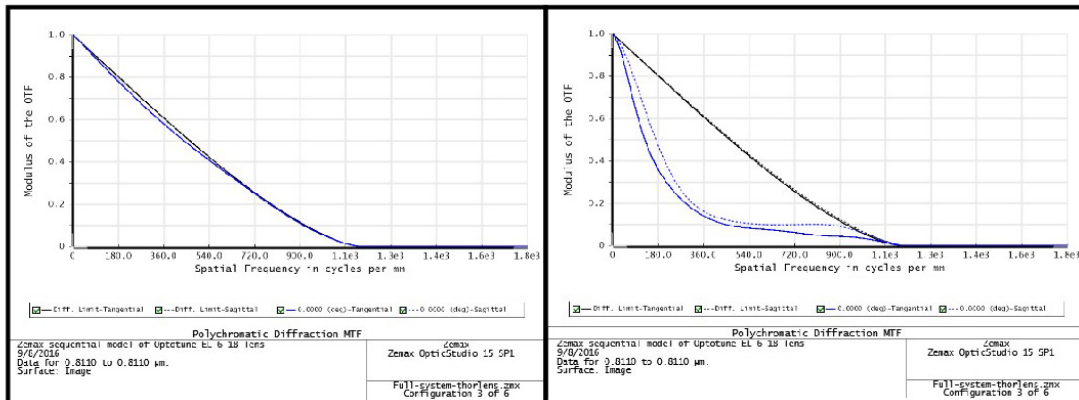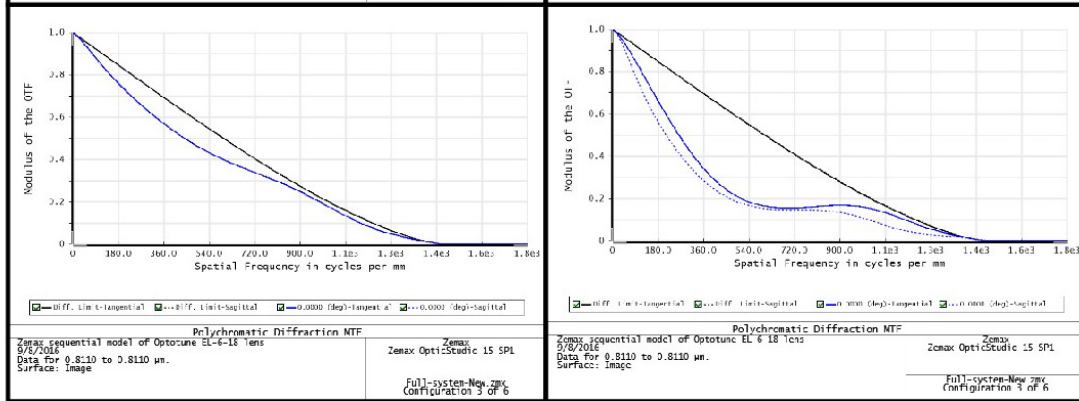
Figure 4.6: Modulation transfer functions of system. (left) MTFs at 0 ţm field. (right) MTFs at 175 ţm field. (A) Original system at 65 ţm working distance. (B) New system at 65 ţm working distance.

reflected light is collected by the inner cladding. The double clad fiber allows the use of a partially coherent detection scheme using a single fiber and common illumination and detection path [79]. Since the core and inner cladding inherently lie in the same plane, the illumination and detection planes are automatically aligned, removing the need for time consuming alignment before each imaging session. The double-clad fiber is a custom 2x2 coupler from Castor Optics, which is designed so that the size of the inner cladding to core is a ratio of about 5, the optimum for balancing resolution, speckle reduction, and signal collection [80]. The theoretical axial resolution is 5.7 ţm using the calculation for a partially coherent detector [23].

The collected signal is split into the multi-mode fiber at the coupler then connected to a photomultiplier tube (Hamamatsu, H9305-03). The signal from the photomultiplier tube (PMT) is amplified with a high bandwidth current-to-voltage amplifier (Hamamatsu, C9999) then digitized by an oscilloscope (National Instruments, PXI-N5122). Acquisition is controlled by a LabVIEW program. Horizontal synchronization is achieved by using the sync signal from the control board of the resonant scanning mirror as the oscilloscope trigger. The vertical synchronization is software timed so that the galvanometer mirror scan and the image frame capture are started together. The program corrects the image for distortion from the non-linear (sine wave) scan of the resonant scanning mirror by resampling the horizontal line with an inverse sine sampling interval. The imaging system was used to collect images in vivo from the oral tissue of healthy volunteers and of patients displaying oral lesions in the clinic. In the clinic, a patient is identified as a candidate for reflectance confocal microscopy and consented by the doctor after standard of care (SOC) diagnosis. Prior to imaging, a gauze pad soaked in 5% acetic acid solution is applied gently to the lesion for 1 minute. The objective lens of the confocal probe is placed in contact with the lesion by the doctor. Image collection is started by an operator and the doctor scans a small area of the lesion. The operator then starts a 5 second full range axial scan

driven by the ETL. Once images are collected of the lesion, the same procedure of acetic acid application and imaging are performed on the contralateral normal tissue. The patient then undergoes a biopsy procedure as SOC. The confocal imaging procedure is performed on the biopsied tissue again and then the tissue is fixed and sent to histology as SOC.

4.3 Results

The axial response was measured by moving a mirror on a translational stage axially through the focus of the microscope. This was repeated at regular intervals of working distance by changing the ETL current. The full width half maximum (FWHM) of the axial response varies over the focal range due to aberration differences and is between 6 ţm and 12 ţm. Although the objective is well corrected for spherical aberration, aberration from the ETL and the coverslip may worsen resolution. It is important to note that the axial response shape shows a large side lobe, or split, which can make measurement difficult [81]. The FWHM can still be estimated by defining the half maximum at either side of the response curve, which gives the largest value for FWHM. Performance may be better than anticipated from these values. At shorter working distances, there is also slight underfilling of the objective. The lenses are nominally designed for infinite conjugates so additional aberration will appear when the ETL changes the divergence. Figure 4.7 shows the axial full width half maximum of the axial response at different working distances for the objective without and with a coverslip. By just shifting the working distances, the optical sectioning ability is improved, even though the coverslip adds aberration. Also notice that in the original design, much of the shorter working distance range had such poor optical sections (on the order of two to four cell layers). The improvements make the difference between resolving cells and not resolving cells. The lateral resolution is shown in Figure 4.8 for multiple working distances when using a coverslip and when not using a coverslip. The improvement when using a coverslip is slight at the short working

48
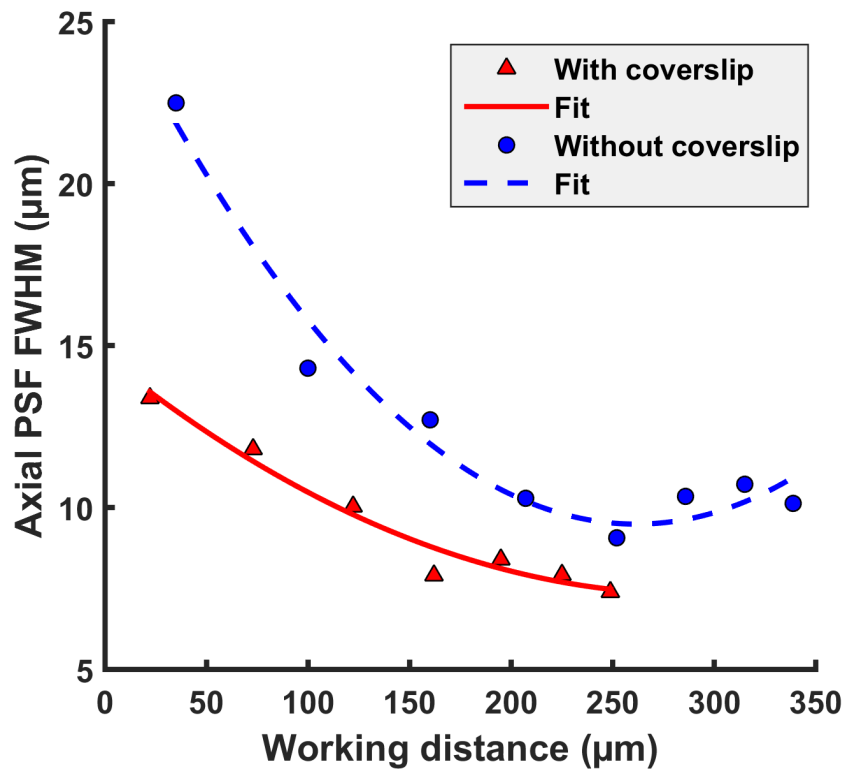
Figure 4.7: Axial response full width half maximum for the system when the objective is covered with a coverslip vs without a coverslip. The working distance is shifted so that zero working distance is the coverslip to water interface when using a coverslip, and the lens to water interface when not using the coverslip.
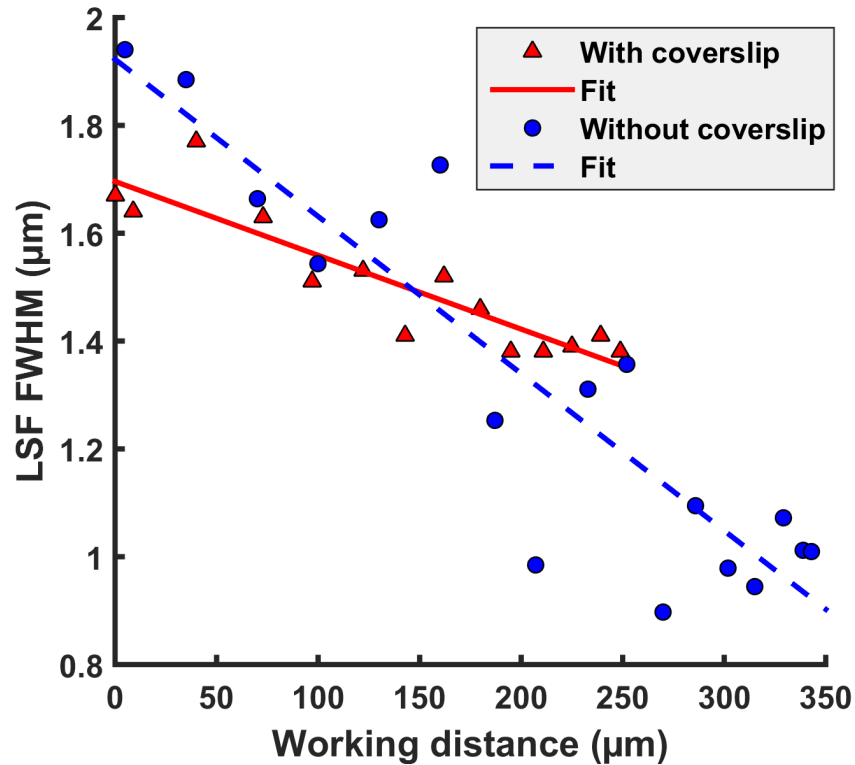
Figure 4.8: Lateral resolution with and without coverslip.

distances, however, at the longer working distances, the resolution is similar or worse likely due to the aberrations introduced by the coverslip. To further verify image quality, a 1951 USAF Resolution Target was imaged at multiple depths. Figure 4.9 shows one depth where group 9 element 3 is resolved. Group 9 element 3 is 645 line pairs per millimeter, or a bar pair width of 1.55 ţm. The Rayleigh criterion for lateral resolution is 0.71 ţm, however, the sampling interval is 0.85 ţm which makes the resolution limit the Nyquist frequency (in the x or y dimension) of 588 lines per mm (1.7 ţm period).

4.4 Conclusion

In conclusion, we present a more robust handheld tunable confocal microendoscope. Fiber alignment is no longer necessary, making resolution and contrast robust against day
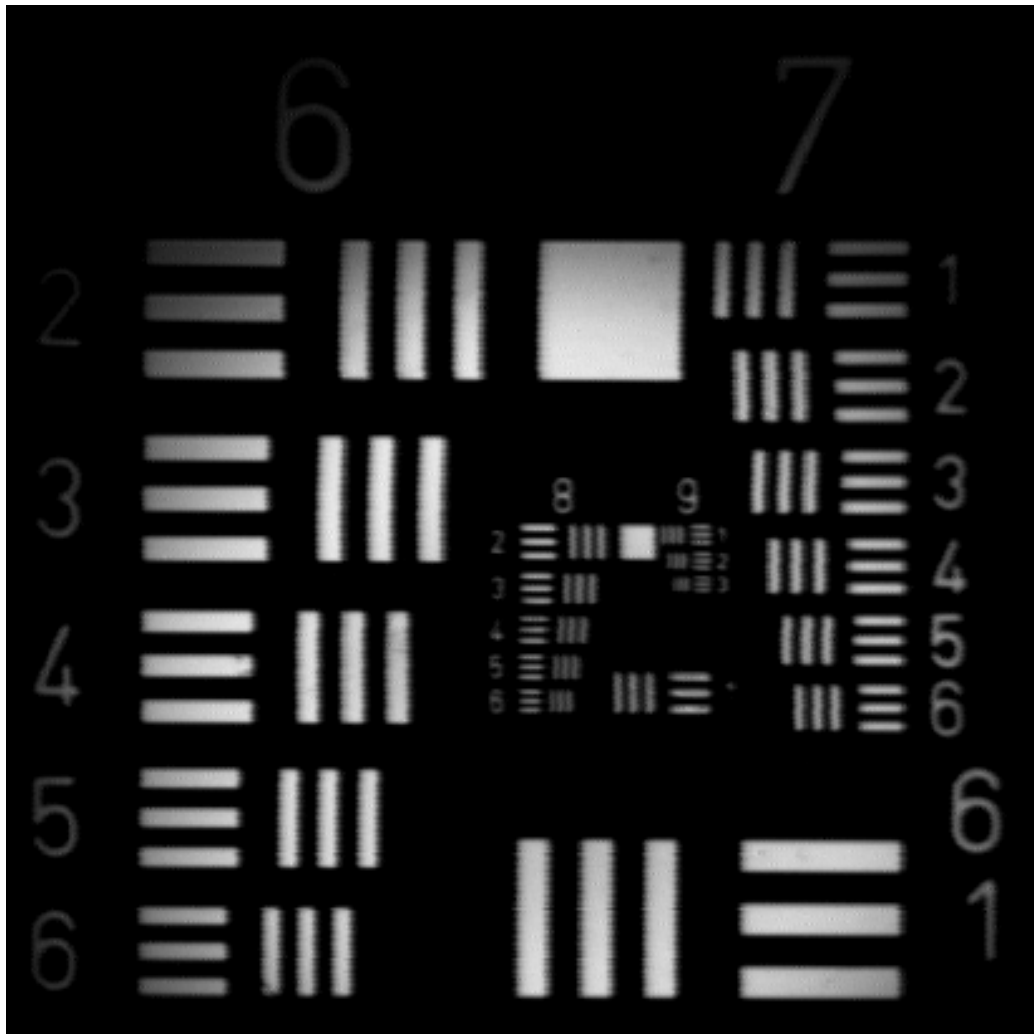
Figure 4.9: 1951 USAF Target.

to day use. The reduction in weight and improvements to the optical quality at short working distances have produced more interesting images, whereas previous scans were often lacking in features such as nuclei due to poor image quality when deviating from the nominal working distance. The images presented in this paper show the importance of resolving nuclei, as they are the dominant feature and indicator of certain pathological morphologies.

5.   IN VIVO HAND-HELD CONFOCAL MICROSCOPY

5.1   Introduction

The introduction of this work highlighted the need for real time in vivo imaging of oral epithelium. This work aimed to offer the ability to fill that need by using innovative scanning technologies and implementing superior design for a robust hand-held confocal microscope. The real test is discussed in this section, where the tunable focus confocal microscope is used in a clinical study to determine the efficacy of the device. Preliminary results are presented and show promising capability of such a device.

5.2   Clinical Study

The clinical study was performed at the Baylor Collge of Dentistry (BCD), part of the Texas A&M Health Science Center, in Dallas, Texas. The tunable focus confocal microscope system was brought to the stomatology clinic at BCD with another system to be tested (a fluorescence lifetime imaging microscope (FLIM) [82]). The images gathered from volunteer patients exhibiting oral lesions are presented here.

5.2.1   Methods

Images were collected from the oral cavity of healthy volunteers and those displaying lesions in the mouth. For the healthy volunteers, several imaging sites were chosen to reflect the capability of the tunable RCM for resolving tissue features and accessing difficult to reach areas. Volunteers with lesions were chosen from patients with scheduled visits to the clinic. If a suspicious lesion was found and a biopsy was ordered as standard of care, then the patient would be asked to volunteer in the study. If the patients agreed, the lesion to be biopsied would be imaged with the FLIM microscope then with the tunable RCM. Afterwards, the patient would continue with the biopsy procedure and the biopsied tissue

would be imaged with the microscopes using the benchtop mounts for the probes. Within 15 minutes, the biopsy would be sent to histology for processsing and diagnosis. A pathology report which is generated as standard of care was then documented for comparison of clinical and histopathological diagnosis to features imaged with the RCM.

The imaging protocol for the tunable RCM is as follows. First the volunteer has 5% acetic acid (vinegar) on a gauze pad applied to the area of interest for one minute. Acetic acid is known to improve the contrast of cell nuclei [67]. After the vinegar application, the probe is placed in contact with the area of interest. Image acquisition is started by the co-operator and images are displayed in real time at 6.6 fps. The operator can now scan the tissue by moving the probe to the side or having the co-operator scan the depth by adjusting the tunable lens settings. If an interesting feature is in the field of view, a full depth scan is initiated by the co-operator. After the final scan, the image acquisition stops and the data is saved to the computer as a video (image sequence of 8-bit images). If the scan was done for a volunteer with a lesion, the lesion is first scanned by the procedure described above, then the healthy contralateral side of the mouth is scanned for a comparison of healthy and lesioned tissue in the same person. Healthy volunteers are only scanned once per session or region of interest as no comparison is necessary.

5.2.2 Preliminary Results

Figure 5.1 shows data from healthy volunteers to illustrate the capability of the probe for in vivo use. The microscope can be used to access several hard to reach areas of the oral cavity. Images are shown of the buccal mucosa of the cheek (Figure 5.1B), the retromolar trigone (Figure 5.1C), the lateral tongue (Figure 5.1D), and the gingiva (Figure 5.1G). Each of these is in the shallow to deep region of the spinous layer. Without the miniature size and reach of the probe, these sites would be difficult or impossible to image. Other features can be seen in the various sites as shown in Figure 5.1 (E,F,H,I). The epithelial junction in
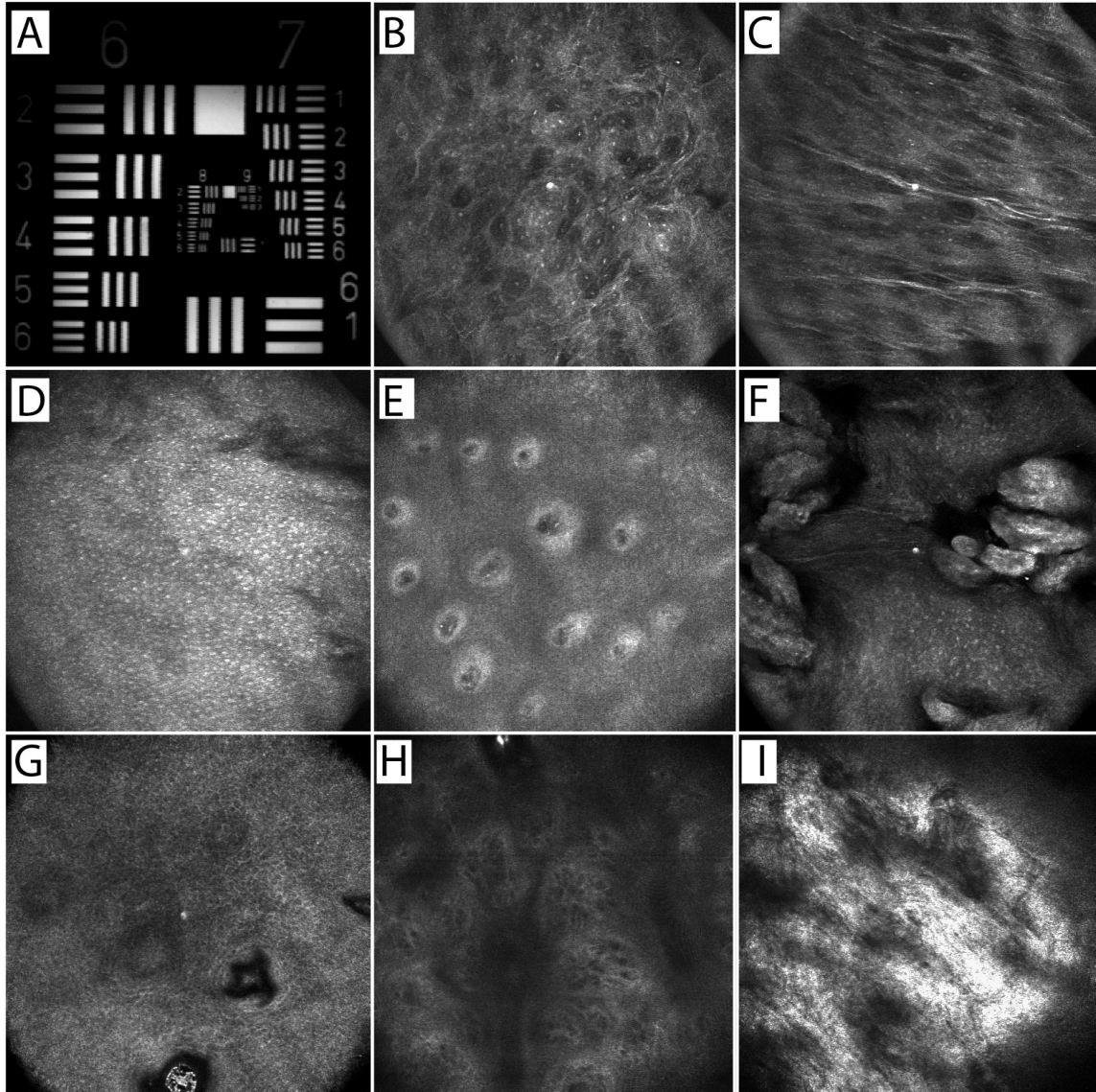
Figure 5.1: Images from healthy volunteers. (A) Air Force Target demonstrating resolution capability and field of view. (B) buccal mucosa. (C) retromolar trigone. (D) tongue shallow. (E) tongue deep. (F) top of tongue. (G-H) gingiva. (I) submucosa of lip.

the tongue exhibits connective tissue papillae and a healthy basal lamina characterized by small, numerous, and structured cells (Figure 5.1E). The image of the top of the tongue shows epithelium with lingual papillae (Figure 5.1G). Blood vessels can be seen in the submucosa of the lip (Figure 5.1H), which demonstrates the large depth range of the probe.

Images captured in vivo are shown in (Figure 5.2) at depths of approximately 75, 100, and 150 ţm into the epithelium, respectively. The cell nuclei are well defined and some cell borders can be seen. The normal tissue shows nuclei approximately 8-10 ţm in diameter and increasing in density with depth. The inflamed tissue has slightly smaller nuclei but are densely crowded together even in the relatively shallow 75 ţm depth range. The deepest image shown for the inflamed tissue is degraded likely due to the increased scattering from the nuclei dense morphology of the shallower tissue. The histopathological diagnosis for this biopsy was chronic inflammation displaying ulcerated mucosa. The histology section in Figure 5.2G shows a separated epithelium and a submucosa invaded by inflammatory cells. These features could be predicted by the confocal images since there was also indication of a lack of epithelial cells and the presence of small crowded nuclei in an unorganized structure, which are characteristic of the inflammatory cells.

5.3   Conclusion

The RCM probe has collected images in vivo from healthy volunteers and from volunteer patients at the stomatology clinic. The results from the healthy volunteers show good resolution and an ability to see characteristic features in several areas of the mouth, including very hard to reach areas such as the retromolar trigone. Early results from patients exhibiting oral lesions are promising. Histological features in the histology section and the RCM images match, such as, lack of epithelium and presence of inflammatory cells. More work will be done to collect images of more and varied lesions.
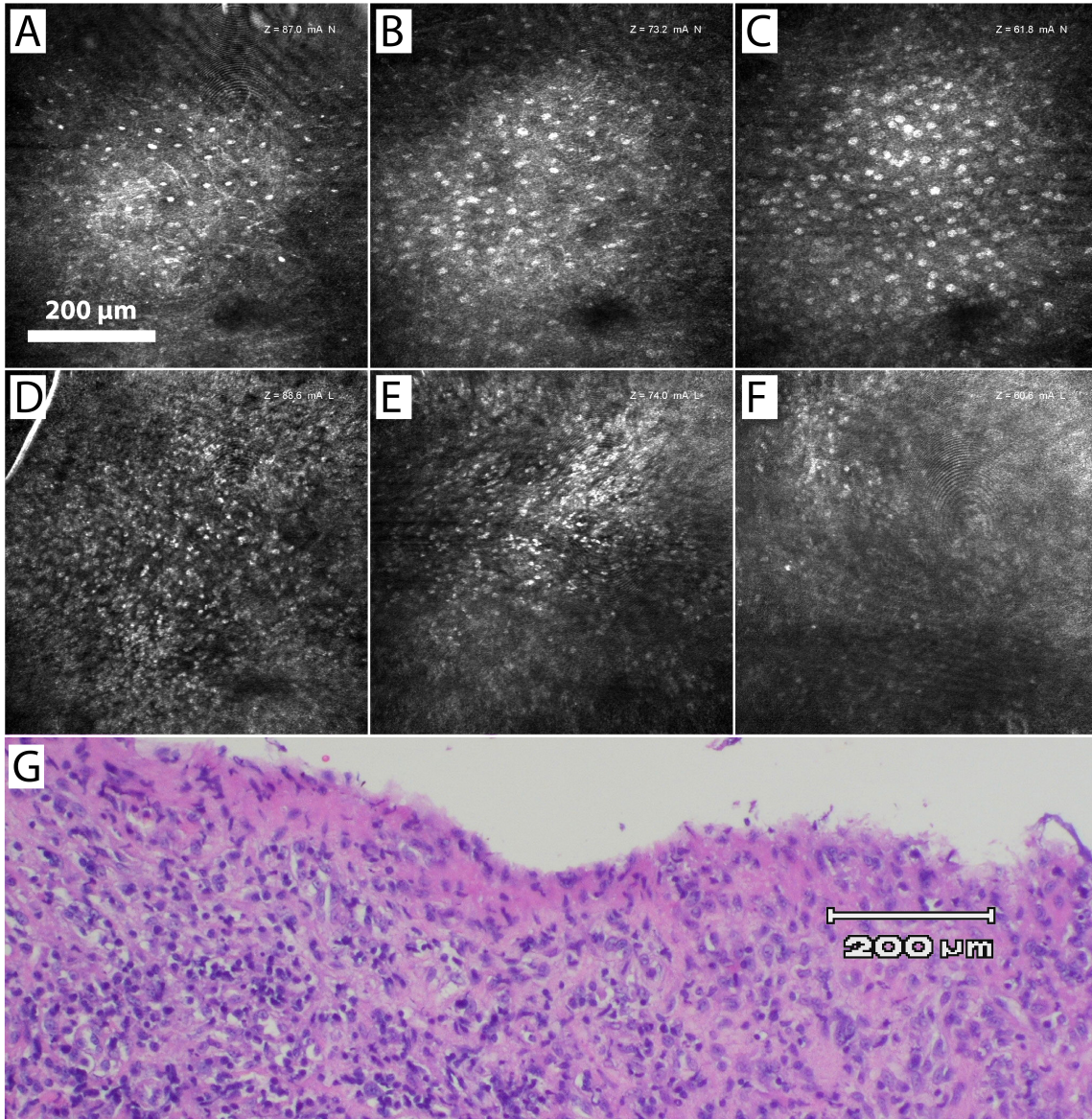
Figure 5.2: RCM images in vivo at a smaller FOV setting. These images are of a lesion exhibiting ulceration. The top images (A-C) are of normal cells on the contralateral side from the lesion. The bottom images (D-F) are of the lesion. (G) A histology section from the processed biopsy

6. SUMMARY AND FUTURE WORK

6.1 Summary

Confocal microscopy has been shown to be useful for imaging the oral cavity, but needs further develop and study [2]. We have shown that non-mechanical axial scanning can improve the capability of RCM as a diagnostic tool. Chromatic confocal microscopy has the potential to collect all depths in a single shot, however, this technique requires more development to increase acquisition speed and reduce price. Tunable RCM is a simple but useful instrument which allows fast focus positioning in vivo and we have shown its efficacy as an imaging device for real time "optical biopsy".

6.2 Future Work

Future work includes further study of the tunable RCM as a diagnostic tool for oral cancer. The work would require more data points across a diverse demographic and varied clinical diagnoses. Quantitative metrics can be utilized, such as nuclear-to-cytoplasmic ratio, or reduced scattering coefficents, to find correlations with specific histopathological diagnoses.

Chromatic confocal microscopy could benefit from specific design such as the custom optics used for the tunable RCM. Additionally, the technique can benefit from development of multiwavelength laser sources and detectors. One such design would utilize discrete wavelengths, instead of a broadband source. This design could have increased speed due to the limited signal collected (less wavelengths) which is limited by the power constraint imposed by the maximum permissible exposure. The most important information may be in only a few depths, which this configuration would provide.

REFERENCES

[1] M. Minsky, "Memoir on inventing the confocal scanning microscope," *Scanning*, vol. 10, no. 4, pp. 128–138, 1988.

[2] A. Lucchese, E. Gentile, A. Romano, C. Maio, L. Laino, and R. Serpico, "The potential role of <i>in vivo</i> reflectance confocal microscopy for evaluating oral cavity lesions: a systematic review," *Journal of Oral Pathology & Medicine*, vol. 45, pp. 723–729, nov 2016.

[3] M. Agozzino, P. Bhasne, C. Franceschini, G. Vincenza, C. Catrical, and M. Ardig, "Noninvasive, in vivo assessment of oral squamous cell carcinoma," mar 2014.

[4] R. L. Siegel, K. D. Miller, and A. Jemal, "Cancer statistics, 2016," *CA: A Cancer Journal for Clinicians*, vol. 66, pp. 7–30, jan 2016.

[5] P. N. Robinson and A. R. Mickelson, "Early diagnosis of oral cavity cancers," *Otolaryngologic Clinics of North America*, vol. 39, no. 2, pp. 295–306, 2006.

[6] K. Kourelis, T. Tsue1, D. Girod, O. Tawfik, K. Sykes, and Y. Shnayder, "Negative prognostic factors for head and neck cancer in the young," *JBUON*, vol. 18, no. 2, pp. 459–64, 2013.

[7] B. Young, P. Woodford, and O. Gerladine, *Functional histology*. 2013.

[8] P. Cancela-Rodríguez, R. Cerero-Lapiedra, G. Esparza-Gómez, S. Llamas-Martínez, and S. Warnakulasuriya, "The use of toluidine blue in the detection of pre-malignant and malignant oral lesions," *Journal of Oral Pathology & Medicine*, vol. 40, pp. 300–304, apr 2011.

[9] K. Onizawa, H. Saginoya, Y. Furuya, H. Yoshida, and H. Fukuda, "Usefulness of fluorescence photography for diagnosis of oral cancer.," *International Journal of Oral and Maxillofacial Surgery*, vol. 28, pp. 206–210, 1999.

[10] S. Cheng, R. M. Cuenca, B. Liu, B. H. Malik, J. M. Jabbour, K. C. Maitland, J. Wright, Y.-S. L. Cheng, and J. a. Jo, "Handheld multispectral fluorescence lifetime imaging system for in vivo applications.," *Biomedical Optics Express*, vol. 5, no. 3, pp. 921–31, 2014.

[11] R. Wessels, D. M. De Bruin, D. J. Faber, T. G. Van Leeuwen, M. Van Beurden, and T. J. M. Ruers, "Optical biopsy of epithelial cancers by optical coherence tomography (OCT)," *Lasers in Medical Science*, vol. 29, pp. 1297–1305, mar 2013.

[12] W. M. White, M. Rajadhyaksha, S. González, R. L. Fabian, and R. R. Anderson, "Noninvasive imaging of human oral mucosa in vivo by confocal reflectance microscopy," *The Laryngoscope*, vol. 109, pp. 1709–1717, oct 1999.

[13] N. G. Maher, H. Collgros, P. Uribe, S. Ch'ng, M. Rajadhyaksha, and P. Guitera, "In vivo confocal microscopy for the oral cavity: Current state of the field and future potential," *Oral Oncology*, vol. 54, pp. 28–35, 2016.

[14] S. Abeytunge, Y. Li, B. Larson, G. Peterson, E. Seltzer, R. Toledo-Crow, and M. Rajadhyaksha, "Confocal microscopy with strip mosaicing for rapid imaging over large areas of excised tissue.," *Journal of Biomedical Optics*, vol. 18, no. 6, p. 61227, 2013.

[15] M. D. Chidley, C. Liang, M. R. Descour, K.-B. Sung, R. R. Richards-Kortum, and A. Gillenwater, "Miniature injection-molded optics for fiber-optic, in vivo confocal microscopy," p. 126, dec 2002.

[16] K. Murakami, A. Murata, T. Suga, H. Kitagawa, Y. Kamiya, M. Kubo, K. Matsumoto, H. Miyajima, and M. Katashiro, "A miniature confocal optical microscope

with MEMS gimbal scanner," in *TRANSDUCERS '03. 12th International Conference on Solid-State Sensors, Actuators and Microsystems. Digest of Technical Papers (Cat. No.03TH8664)*, vol. 1, pp. 587–590, IEEE.

[17] M. Gu and D. Bird, "Fibre-optic double-pass confocal microscopy," *Optics & Laser Technology*, vol. 30, pp. 91–93, mar 1998.

[18] V. Dubaj, A. Mazzolini, A. Wood, and M. Harris, "Optic fibre bundle contact imaging probe employing a laser scanning confocal microscope," *Journal of Microscopy*, vol. 207, pp. 108–117, aug 2002.

[19] M. Minsky, "Microscopy apparatus," 1961.

[20] P. Davidovits and M. D. Egger, "Scanning laser microscope for biological investigations.," *Applied Optics*, vol. 10, no. 7, pp. 1615–1619, 1971.

[21] M. Gu, C. J. R. Sheppard, and X. Gan, "Image formation in a fiber-optical confocal scanning microscope," *The Journal of the Optical Society of America*, vol. 8, no. 11, pp. 1755–1761, 1991.

[22] T. Wilson and C. J. R. Sheppard, *Theory and practice of scanning optical microscopy.* 1984.

[23] T. Wilson and a. R. Carlini, "Size of the detector in confocal imaging systems.," *Optics Letters*, vol. 12, no. 4, pp. 227–229, 1987.

[24] G. Q. Xiao, T. R. Corle, and G. S. Kino, "Real-time confocal scanning optical microscope," *Applied Physics Letters*, vol. 53, no. 8, p. 716, 1988.

[25] K.-B. Im, S. Han, H. Park, D. Kim, and B.-M. Kim, "Simple high-speed confocal line-scanning microscope," *Optics Express*, vol. 13, no. 13, p. 5151, 2005.

[26] S. Kim, J. Hwang, J. Heo, S. Ryu, D. Lee, S.-H. Kim, S. J. Oh, and C. Joo, "Spectrally encoded slit confocal microscopy using a wavelength-swept laser," *Journal of Biomedical Optics*, vol. 20, p. 036016, mar 2015.

[27] S. Abeytunge, Y. Li, B. Larson, R. Toledo-Crow, and M. Rajadhyaksha, "Rapid confocal imaging of large areas of excised tissue with strip mosaicing.," *Journal of Biomedical Optics*, vol. 16, p. 050504, may 2011.

[28] M. A. Saldua, C. A. Olsovsky, E. S. Callaway, R. S. Chapkin, and K. C. Maitland, "Imaging inflammation in mouse colon using a rapid stage-scanning confocal fluorescence microscope.," *Journal of Biomedical Optics*, vol. 17, no. 1, p. 016006, 2012.

[29] G. J. Tearney, R. H. Webb, and B. E. Bouma, "Spectrally encoded confocal microscopy," *Optics Letters*, vol. 23, p. 1152, aug 1998.

[30] D. Mendlovic, J. Garcia, Z. Zalevsky, E. Marom, D. Mas, C. Ferreira, and A. W. Lohmann, "Wavelength-multiplexing system for single-mode image transmission," *Applied Optics*, vol. 36, p. 8474, nov 1997.

[31] G. J. Tearney, M. Shishkov, and B. E. Bouma, "Spectrally encoded miniature endoscopy," *Optics Letters*, vol. 27, p. 412, mar 2002.

[32] S. C. Schlachter, D. Kang, M. J. Gora, P. Vacas-Jacques, T. Wu, R. W. Carruth, E. J. Wilsterman, B. E. Bouma, K. Woods, and G. J. Tearney, "Spectrally encoded confocal microscopy of esophageal tissues at 100 kHz line rate," *Biomedical Optics Express*, vol. 4, p. 1636, sep 2013.

[33] C. Pitris, B. Bouma, M. Shiskov, and G. Tearney, "A GRISM-based probe for spectrally encoded confocal microscopy," *Optics Express*, vol. 11, p. 120, jan 2003.

[34] D. J. Mar, J. P. Marsh, C. P. Deen, H. Ling, H. Choo, and D. T. Jaffe, "Micromachined silicon grisms for infrared optics," *Applied Optics*, vol. 48, p. 1016, feb 2009.

[35] Y. K. Tao and J. A. Izatt, "Spectrally encoded confocal scanning laser ophthalmoscopy," *Optics Letters*, vol. 35, p. 574, feb 2010.

[36] E. F. Brachtel, N. B. Johnson, A. E. Huck, T. L. Rice-Stitt, M. G. Vangel, B. L. Smith, G. J. Tearney, and D. Kang, "Spectrally encoded confocal microscopy for diagnosing breast cancer in excision and margin specimens," *Laboratory Investigation*, vol. 96, pp. 459–467, apr 2016.

[37] T. D. Wang, M. J. Mandella, C. H. Contag, and G. S. Kino, "Dual-axis confocal microscope for high-resolution in vivo imaging," *Optics Letters*, vol. 28, p. 414, mar 2003.

[38] Y. Chen, D. Wang, A. Khan, Y. Wang, S. Borwege, N. Sanai, and J. T. C. Liu, "Video-rate <i>in vivo</i> fluorescence imaging with a line-scanned dual-axis confocal microscope," *Journal of Biomedical Optics*, vol. 20, p. 106011, oct 2015.

[39] C. Yin, A. Glaser, S. Y. Leigh, Y. Chen, L. Wei, P. C. S. Pillai, M. C. Rosenberg, S. Abeytunge, G. Peterson, C. Glazowski, N. Sanai, M. J. Mandella, M. Rajadhyaksha, and J. T. C. Liu, "Miniature in vivo MEMS-based line-scanned dual-axis confocal microscope for point-of-care pathology," *Biomedical Optics Express*, vol. 7, p. 251, feb 2016.

[40] J. Choi, Z. Qiu, C.-H. Rhee, T. D. Wang, and K. R. Oldham, "A novel piezoelectric microstage with embedded sensor for dual axes confocal endomicroscopy (Conference Presentation)," p. 96910A, apr 2016.

[41] B. Larson, S. Abeytunge, and M. Rajadhyaksha, "Performance of full-pupil line-scanning reflectance confocal microscopy in human skin and oral mucosa in vivo," *Biomedical Optics Express*, vol. 2, no. 7, pp. 2055–67, 2011.

[42] S. Kim, J. Hwang, J. Heo, S. Ryu, D. Lee, S.-H. Kim, S. J. Oh, and C. Joo, "Spectrally encoded slit confocal microscopy using a wavelength-swept laser," *Journal of Biomedical Optics*, vol. 20, p. 036016, mar 2015.

[43] D. Wang, Y. Chen, Y. Wang, and J. T. C. Liu, "Comparison of line-scanned and point-scanned dual-axis confocal microscope performance," *Optics Letters*, vol. 38, p. 5280, dec 2013.

[44] C. L. Arrasmith, D. L. Dickensheets, and A. Mahadevan-Jansen, "MEMS-based handheld confocal microscope for in-vivo skin imaging.," *Optics Express*, vol. 18, no. 4, pp. 3805–3819, 2010.

[45] S. Cha, P. C. Lin, L. Zhu, P. C. Sun, and Y. Fainman, "Nontranslational three-dimensional profilometry by chromatic confocal microscopy with dynamically configurable micromirror scanning.," *Applied Optics*, vol. 39, no. 16, pp. 2605–2613, 2000.

[46] J. Knittel, L. Schnieder, G. Buess, B. Messerschmidt, and T. Possner, "Endoscope-compatible confocal microscope using a gradient index-lens system," *Optics Communications*, vol. 188, no. 5-6, pp. 267–273, 2001.

[47] K. B. Sung, C. Liang, M. Descour, T. Collier, M. Follen, and R. Richards-Kortum, "Fiber-optic confocal reflectance microscope with miniature objective for in vivo imaging of human tissues," *IEEE Transactions on Biomedical Engineering*, vol. 49, no. 10, pp. 1168–1172, 2002.

[48] A. a. Tanbakuchi, A. R. Rouse, J. a. Udovich, K. D. Hatch, and A. F. Gmitro, "Clinical confocal microlaparoscope for real-time in vivo optical biopsies.," *Journal of Biomedical Optics*, vol. 14, no. 4, p. 044030, 2014.

[49] C. Olsovsky, R. Shelton, O. Carrasco-Zevallos, B. E. Applegate, and K. C. Maitland, "Chromatic confocal microscopy for multi-depth imaging of epithelial tissue," *Biomedical Optics Express*, vol. 4, no. 5, pp. 732–740, 2013.

[50] a. K. Dunn, C. Smithpeter, a. J. Welch, and R. Richards-Kortum, "Sources of contrast in confocal reflectance imaging.," *Applied ?Optics*, vol. 35, no. 19, pp. 3441–3446, 1996.

[51] C. L. Smithpeter, a. K. Dunn, a. J. Welch, and R. Richards-Kortum, "Penetration depth limits of in vivo confocal reflectance imaging.," *Applied Optics*, vol. 37, no. 13, pp. 2749–2754, 1998.

[52] I. Veilleux, J. Spencer, D. Biss, D. Cote, and C. Lin, "In vivo cell tracking with video rate multimodality laser scanning microscopy," *IEEE Journal of Selected Topics in Quantum Electronics*, vol. 14, no. 1, pp. 10–18, 2008.

[53] Y. S. Sabharwal, A. R. Rouse, L. Donaldson, M. F. Hopkins, and A. F. Gmitro, "Slit-scanning confocal microendoscope for high-resolution in vivo imaging.," *Applied Optics*, vol. 38, no. 34, pp. 7133–7144, 1999.

[54] C. Boudoux, S. Yun, W. Oh, W. White, N. Iftimia, M. Shishkov, B. Bouma, and G. Tearney, "Rapid wavelength-swept spectrally encoded confocal microscopy.," *Op-tics Express*, vol. 13, no. 20, pp. 8214–8221, 2005.

[55] J. Garzón, T. Gharbi, and J. Meneses, "Real time determination of the optical thick-ness and topography of tissues by chromatic confocal microscopy," *Journal of Optics A: Pure and Applied Optics*, vol. 10, no. 10, p. 104028, 2008.

[56] P. M. Lane, R. P. Elliott, and C. E. MacAulay, "Confocal microendoscopy with chro-matic sectioning," *Spectral Imaging: Instrumentation, Applications, and Analysis II*, vol. 4959, pp. 23–26, 2003.

[57] H. J. Tiziani and H. M. Uhde, "Three-dimensional image sensing by chromatic con-focal microscopy.," *Applied Optics*, vol. 33, no. 10, pp. 1838–1843, 1994.

[58] K. Shi, P. Li, S. Yin, and Z. Liu, "Chromatic confocal microscopy using supercontinuum light.," *Optics Express*, vol. 12, no. 10, pp. 2096–2101, 2004.

[59] G. Li, P. C. Sun, P. C. Lin, and Y. Fainman, "Interference microscopy for three-dimensional imaging with wavelength-to-depth encoding.," *Optics Letters*, vol. 25, no. 20, pp. 1505–7, 2000.

[60] B. S. Chun, K. Kim, and D. Gweon, "Three-dimensional surface profile measurement using a beam scanning chromatic confocal microscope.," *The Review of Scientific Instruments*, vol. 80, no. 7, p. 073706, 2009.

[61] Q. Xu, K. Shi, S. Yin, and Z. Liu, "Chromatic two photon imaging," in *2008 Conference on Quantum Electronics and Laser Science Conference on Lasers and Electro-Optics, CLEO/QELS*, 2008.

[62] Z. Ding, H. Ren, Y. Zhao, J. S. Nelson, and Z. Chen, "High-resolution optical coherence tomography over a large depth range with an axicon lens.," *Optics Letters*, vol. 27, no. 4, pp. 243–245, 2002.

[63] M. A. Browne, O. Akinyemi, and A. Boyde, "Confocal surface profiling utilizing chromatic aberration," *Scanning*, vol. 14, pp. 145–153, 1992.

[64] V. Tombelaine, C. Lesvigne, P. Leproux, L. Grossard, V. Couderc, J.-L. Auguste, J.-M. Blondy, G. Huss, and P.-H. Pioger, "Ultra wide band supercontinuum generation in air-silica holey fibers by SHG-induced modulation instabilities.," *Optics Express*, vol. 13, no. 19, pp. 7399–7404, 2005.

[65] A. K. Ruprecht, T. F. Wiesendanger, and H. J. Tiziani, "Chromatic confocal microscopy with a finite pinhole size.," *Optics Letters*, vol. 29, no. 18, pp. 2130–2132, 2004.

[66] M. Vaishakh, "Optical sectioning in reciprocal fiber-optic based chromatic confocal microscope," *Optik*, vol. 123, no. 16, pp. 1450–1452, 2012.

[67] T. Collier, P. Shen, B. de Pradier, K. B. Sung, R. Richards-Kortum, M. Follen, and a. Malpica, "Near real time confocal microscopy of amelanotic tissue: dynamics of aceto-whitening enable nuclear segmentation.," *Optics Express*, vol. 6, no. 2, pp. 40–48, 2000.

[68] C. Yang, K. Shi, H. Li, Q. Xu, V. Gopalan, and Z. Liu, "Chromatic second harmonic imaging.," *Optics Express*, vol. 18, no. 23, pp. 23837–43, 2010.

[69] M. Strupler, E. De Montigny, D. Morneau, and C. Boudoux, "Rapid spectrally encoded fluorescence imaging using a wavelength-swept source.," *Optics Letters*, vol. 35, no. 11, pp. 1737–9, 2010.

[70] J. Novak and A. Miks, "Hyperchromats with linear dependence of longitudinal chromatic aberration on wavelength," *Optik*, vol. 116, no. 4, pp. 165–168, 2005.

[71] J.Dyson, "Circular and spiral diffraction grating," *Proceedings of the Royal Society of London. Series A, Mathematical and Physical Sciences*, vol. 387, no. 1792, pp. 133–146, 1983.

[72] C. J. R. Sheppard, X. Gan, M. Gu, and M. Roy, "Signal-to-noise ratio in confocal microscopes," in *Handbook of Biological Confocal Microscopy: Third Edition*, pp. 442–452, 2006.

[73] L. I. A. Laser Institute of America, "ANSI Z136.1: American National Standard for Safe Use of Lasers," *SPIE Medical Imaging*, p. 90400Q, 2007.

[74] J. B. Pawley and B. R. Masters, *Handbook of Biological Confocal Microscopy, Third Edition*, vol. 13. 2008.

[75] P. C. Lin, P. C. Sun, L. Zhu, and Y. Fainman, "Single-shot depth-section imaging through chromatic slit-scan confocal microscopy.," *Applied Optics*, vol. 37, no. 28, pp. 6764–6770, 1998.

[76] L. Yang, A. Mac Raighne, E. M. McCabe, L. A. Dunbar, and T. Scharf, "Confocal microscopy using variable-focal-length microlenses and an optical fiber bundle.," *Applied Optics*, vol. 44, no. 28, pp. 5928–5936, 2005.

[77] J. M. Jabbour, B. H. Malik, C. Olsovsky, R. Cuenca, S. Cheng, J. A. Jo, Y.-S. L. Cheng, J. M. Wright, and K. C. Maitland, "Optical axial scanning in confocal microscopy using an electrically tunable lens," *Biomedical Optics Express*, vol. 5, no. 2, pp. 645–652, 2014.

[78] J. M. Jabbour, J. L. Bentley, B. H. Malik, J. Nemechek, J. Warda, R. Cuenca, S. Cheng, J. a. Jo, and K. C. Maitland, "Reflectance confocal endomicroscope with optical axial scanning for in vivo imaging of the oral mucosa.," *Biomedical Optics Express*, vol. 5, no. 11, pp. 3781–91, 2014.

[79] D. Yelin, B. E. Bouma, S. H. Yun, and G. J. Tearney, "Double-clad fiber for endoscopy.," *Optics Letters*, vol. 29, no. 20, pp. 2408–10, 2004.

[80] E. De Montigny, W.-J. Madore, O. Ouellette, G. Bernard, M. Leduc, M. Strupler, C. Boudoux, and N. Godbout, "Double-clad fiber coupler for partially coherent detection.," *Optics Express*, vol. 23, pp. 9040–51, apr 2015.

[81] T. Wilson and A. R. Carlini, "The effect of aberrations on the axial response of con-focal imaging systems," *Journal of Microscopy*, vol. 154, no. July 1988, pp. 243–256, 1989.

[82] J. M. Jabbour, S. Cheng, B. H. Malik, R. Cuenca, J. A. Jo, J. Wright, Y.-S. L. Cheng, and K. C. Maitland, "Fluorescence lifetime imaging and reflectance confocal mi-

croscopy for multiscale imaging of oral precancer.," *Journal of Biomedical Optics*, vol. 18, no. 4, p. 046012, 2013.

APPENDIX A

MISCELLANEOUS

A.1   Matlab Code for Determining Confocal Resolution

The following code is written in Matlab. It describes the procedure for calculating the three dimensional point spread function using a Fourier Optics method.

```matlab
%%% Calculating the theoretical resolution of confocal microscopy
% From Wilson & Sheppard, the point spread function is h(u,v) with
% optical coordinates u and v which are defined as u =
% k*z*sin^2(alpha) and v = k*r*sin(alpha)

% Create mesh
u = linspace(0,50,100);
v = linspace(0.01,20,200);
rho = linspace(0,1,200);
[U V RHO] = meshgrid(u,v,rho);

% Define the point spread function
% h(u,v) = int_0^1 {P(rho) exp(1/2 j u rho^2) J0(u v)} rho drho
drho = mean(diff(rho)); % for integration
h = trapz(exp(1i/2*U.*RHO.^2).*besselj(0,V.*RHO).*RHO,3)*drho;

%% Axial half width half maximum
% I(u) = int_0^vp |h(2u,v)|^2 vdv
vp = 0.1:.2:15; clear uh
for i = 1:length(vp)
    tic;
```

```matlab
    % Create mesh
    [U V] = meshgrid(u,v);


    % Calculate the intensity versus axial position
    I_u = sum((abs(h).^2.*V).*(V<vp(i)),1);


    % Find half maximum by iterating the interpolant of I
    I_u = I_u./max(I_u); plot(u,I_u); drawnow
    k = 0; while interp1(u,I_u,k)>0.5; k = k+0.01; end;


    % Originally a function of 2u, so we take 1/2 of result
    uh(i) = k/2;


    toc*(length(vp)-i)
end


%% Plot a smoothed graph
vpi = 0:0.01:15;
smooth = spline(vp,uh,vpi);


fig = figure(1);
pl = plot(vpi,smooth);
ax = gca; grid on;
xlabel('$v_p$','interpreter','Latex');
tst=ylabel('$u_{\frac{1}{2}}$','rot',0,'pos', ...
[-1.5 7.5],'interpreter','Latex');
title({'Half width of axial response', 'versus pinhole size'})
pl.LineWidth = 2;
ax.XTick = 0:2:14; ax.YTick = 0:2:14; ax.YLim = [0 15]; axis square
ax.FontSize = 14;
```

```matlab
%% Lateral half width half maximum
clear hwhm sm

% Create mesh (plane in focus)
x = linspace(-10,10,400);
[X Y] = meshgrid(x,x);
R = sqrt(X.^2+Y.^2);

% Solution to point spread function at the focus J1(v)/v
hv = besselj(1,R)./R; hv = hv./max(hv(:));

% Find half width for all vp
vp = 0.05:0.05:10;
tic
for i = 1:length(vp);

    % Define normalized pinhole
    ph = R<vp(i);

    % Confocal intensity is PSF*[PSF(X)D] where (X) is convolution
    final=hv.^2.*conv2(double(ph),hv.^2,'same');

    % Collect intensity for confocal signal level
    sm(i) = sum(final(:));

    % Normalize data for finding half width
    dat = final(:,end/2)./max(final(:));
    % Find half width
    j = 0;
    while interp1(X(end/2,:),dat,j)>0.5
```

72

```
        j = j+0.01;
    end

    hwhm(i) = j;
end
toc


%% Plot smoothed data
vpi = 0:.1:10;
smooth = spline(vp,hwhm,vpi);


fig = figure(2);
pl = plot(vpi,smooth);
ax = gca; grid on;
xlabel('$v_p$','interpreter','Latex');
tst=ylabel('$v_{\frac{1}{2}}$','rot',0,'pos', ...
[-1 1],'interpreter','Latex');
title({'Half width of point', 'versus pinhole size'})
pl.LineWidth = 2;
ax.XTick = 0:2:10; ax.YTick = 0:0.2:2; ax.YLim = [0 2];
axis square
ax.FontSize = 14;
```

A.2 Lens Prescriptions for the Tunable Confocal Microscope

The lens prescription for the objective is listed in Table A.2. The lens prescription for the relay lens is lited in Table A.2

Table A.1: Lens prescription for miniature objective lens. Units in mm.

| OBJ | Radius of Curvature | | Thickness | Aperture diameter | | Glass |
	Front	Back		Front	Back	
1	11.5916 CX	-10.1466 CX	3.0000	7.0000	6.7955	NSK14
2	-10.1466 CC	INF	1.5000	6.7955	6.6288	NSF4
			0.3			
3	7.7830 CX	14.2222 CC	2.5000	6.4886	6.0000	NLAK12
			3.6490			
4	2.3500 CX	INF	3.0000	3.6034	1.1602	NLAK10
5	INF	INF	0.1500	1.1602	0.9269	Nexterion D
6	INF	INF	0.1700			Water

Table A.2: Lens prescription for relay lens. Units in mm.

| OBJ | Radius of Curvature | | Thickness | Aperture diameter | | Glass |
	Front	Back		Front	Back	
1	20.7150 CX	-9.9730 CX	6.5000	6.3500	6.3500	NLAK22
2	-9.9730 CC	-31.3420	2.0000	6.3500	6.3500	NSF6
			67.3			
3	110.7020 CX	20.667 CC	2.5000	6.3500	6.35000	NLAK12
4	20.667 CX	-34.6150 CX	3.0000	3.6034	1.1602	NLAK10